Title: In vivo mapping of striatal microstructure in Huntington's disease with Soma and Neurite Density Imaging

Running title: SANDI in Huntington's disease

Authors: Vasileios Ioakeimidis[1,2], Marco Palombo[2], Chiara Casella[3], Carolyn B. McNabb[2], Robin Schubert[4], Philip Pallmann[5], Monica E. Busse[5], Cheney J. G. Drew[5], Sundus Alusi[6], Timothy Harrower[7], Anne E. Rosser[8,9] & Claudia Metzler-Baddeley[2]

Author affiliations:

[1]Danish Research Centre for Magnetic Resonance, Department for Radiology and Nuclear Medicine, Copenhagen University Hospital Amager and Hvidovre, Copenhagen, Denmark.

[2]Cardiff University Brain Research Imaging Centre (CUBRIC), School of Psychology, Cardiff University, Maindy Road, Cathays, Cardiff, UK.

[3]Department of Perinatal Imaging and Health, School of Biomedical Engineering & Imaging Sciences, King's College London, London, UK.

[4]George Huntington Institut (GHI), Wilhelm-Schickard-Strasse 15, 48149 Muenster, Germany.

[5]Centre for Trials Research, School of Medicine, Cardiff University, Heath Park Way, Cardiff, UK.

[6]The Walton Centre for Neurology and Neurosurgery, Lower Lane, Fazakerley, Liverpool, UK.

[7]Royal Devon and Exeter NHS Trust, Barrack Road, Exeter, UK.

[8]Cardiff University Brain Repair Group, School of Biosciences, Cardiff University, Museum Avenue, Cardiff, UK.

[9]Advanced Neurotherapeutics Centre (ANTC), Department of Neurology and Psychological Medicine, School of Medicine, Cardiff University, Hadyn Ellis Building, Cardiff, UK.

Abstract

Background:
Huntington's Disease (HD) is an inherited neurodegenerative disorder characterised by progressive cognitive and motor decline largely due to the loss of striatal medium spiny neurons in the basal ganglia. No disease-modifying therapies exist, but novel clinical trials are ongoing. Non-invasive imaging biomarkers sensitive to HD neuropathology are essential for evaluating therapeutic effects. Soma and Neurite Density Imaging (SANDI), a multi-shell diffusion-weighted imaging model, estimates intracellular signal fractions from sphere-shaped soma in grey matter. SANDI-derived apparent soma density and size in the striatum have potential as proxies for HD-related neurodegeneration.

Objective:
To characterise HD-related microstructural abnormalities in the basal ganglia using SANDI and examine associations between SANDI indices, volumetric measurements, and motor performance.

Methods:
T1-weighted anatomical and multi-shell diffusion-weighted images (b-values: 200–6,000 s/mm²) were acquired using a 3T Siemens Connectom scanner (300mT/m) in 56 HD gene-positive individuals (41 premanifest) ($Mean_{Age}$ = 46.1, SD_{Age} = 13.8, 25 females) and 57 healthy controls ($Mean_{Age}$ = 45.0, SD_{Age} = 13.8, 31 females). Gene-positive participants completed Quantitative Motor (Q-Motor) tasks, including speeded and paced finger tapping, which were reduced to one motor performance component. Following standard diffusion-weighted data preprocessing, SANDI and diffusion tensor models estimated apparent soma density, soma size, neurite density, extracellular signal fraction, fractional anisotropy, and mean diffusivity. The caudate, putamen, pallidum, and thalamus were segmented bilaterally, and microstructural and volumetric indices were extracted and compared. Correlations between SANDI indices, Q-Motor performance, and volumetric measures were analysed.

Results:
HD was associated with reduced apparent soma density ($r = 0.32$, $p \leq 0.007$) and increased apparent soma size ($r = -0.45$, $p < 0.001$) and extracellular signal fraction ($r = -0.34$, $p \leq 0.003$) in the basal ganglia, but not the thalami. No differences were found in apparent neurite density ($r = -0.18$, $p = 0.17$). Previously reported HD-related increases in fractional

anisotropy and mean diffusivity in the basal ganglia were replicated. Q-Motor component scores correlated negatively with apparent soma density and positively with soma size and extracellular signal fraction. SANDI indices and age explained up to 63% of striatal atrophy in HD.

Conclusion:
SANDI measures detected HD-related neurodegeneration in the striatum, accounted significantly for striatal atrophy, and correlated with motor impairments. Decreased apparent soma density and increased soma size align with *ex vivo* evidence of medium spiny neuron loss and glial reactivity. SANDI shows promise as an *in vivo* biomarker and surrogate outcome measure for HD-related neurodegeneration in clinical trials.

Keywords: Huntington's disease (HD), basal ganglia, grey matter microstructure, Soma and Neurite Density Imaging (SANDI), ultra-strong gradient diffusion-weighted MRI, motor performance

Introduction

Huntington's disease (HD) is an autosomal dominantly inherited neurodegenerative disorder caused by a pathogenic CAG repeat expansion of the Huntingtin gene.[1] HD is characterised by a progressive loss of cognitive and motor functions as well as psychiatric disturbances. The clinical onset of HD is commonly defined by the manifestation of motor symptoms, such as chorea, reduced voluntary motor control, bradykinesia, and difficulty maintaining rhythmic and paced movements.[2–4] However, changes in the brain, notably striatal atrophy in the basal ganglia[5,6] may precede the motor onset by up to 24[7] years[8–10] and correlate with motor and cognitive decline.[2,5,6,11–15]

There is presently no approved disease-modifying therapy for HD, but numerous clinical trials are underway to test the safety and efficacy of novel therapeutics.[16] The recent surge in potential disease-modifying targets has generated a demand for surrogate outcome measures that are sensitive to HD neuropathology and allow a mechanistic assessment of therapeutic effects on striatal neurodegeneration in a timely manner. Volumetric measurements from non-invasive MRI are known to be sensitive to disease progression[17–20] and have been adopted into the recently published Huntington's Disease Integrated Staging System (HD-ISS).[21] However, volumetric measurements do not provide information about the underlying neuropathological tissue changes that lead to striatal atrophy, such as the loss of medium spiny neurons (MSN)[22,23] and changes in glia cell density and morphology, including enlargement of reactive astrocytes and microglia.[22,24–26]

Diffusion-weighted Imaging (DWI) is widely used to investigate brain tissue microstructure in vivo by exploiting apparent water displacement due to Brownian motion.[28,29] Most DWI studies in HD have used diffusion tensor imaging (DTI), which models extra-cellular water diffusion as a Gaussian tensor and measures diffusion properties such as mean diffusivity (MD) and the degree of diffusion anisotropy (fractional anisotropy; FA).[30] DTI studies in HD have consistently reported increases in MD and FA in striatal grey matter,[31,32] that likely arise from the selective neurodegeneration of medium spiny neuron connections.

Advances in multi-shell and ultra-strong gradient DWI,[33] have enabled increasingly sophisticated biophysical models that require data acquisition over a range of b-values to separate extra- from intracellular diffusion signals.[34–36] Several approaches that model intra-neurite space with cylinders or sticks have been put forward (e.g. Composite and Restricted

Model of Diffusion, CHARMED[34]; Convex optimization modelling for microstructure informed tractography; COMMIT[37]; Neurite Orientation Dispersion and Density Index; NODDI[35]). NODDI studies in premanifest HD have revealed reduced apparent neurite density in white mater with localised reductions in fibre orientation dispersion in the corpus callosum and basal ganglia capsules.[38] However, despite putamen volume loss, no NODDI-based differences in striatal grey matter were detected in gene-positive individuals long before motor onset.[7]

Soma And Neurite Density Imaging (SANDI)[27] is a novel biophysical diffusion model that extends multi-compartment approaches like NODDI to account for the more complex geometrical architecture of grey matter. SANDI requires multi-shell acquisition protocols with b-values over 3,000 s/mm^2 to capture restricted signal fractions from within grey matter soma, which are modelled as geometrical spheres. In this way, SANDI provides estimates of apparent soma density (f_{is}) and soma radius (r_s) in addition to apparent neurite density (f_{in}) (modelled with sticks), extracellular signal fraction (f_{ec}) and extracellular diffusivity (D_e). SANDI has been shown to provide highly reproducible and repeatable parameter estimation across grey matter regions in the human brain[39] that align closely with its known cyto- and myeloarchitecture. For instance, the gradients of apparent soma density maps were found to closely match those of Brodmann areas in human cortical regions with different soma density profiles,[27] and correlated in the mouse brain with cell density distributions from the Allen atlas.[27,40] These findings suggest the potential of the SANDI model for quantifying neurodegenerative processes in the grey matter of the living human brain.

Clinical applications of SANDI are currently limited to multiple sclerosis (MS), where reductions in apparent soma and neurite density and increases in extracellular signal fraction in grey and white matter align with MS-related demyelination, axonal loss, and neurodegeneration.[41,42] These microstructural abnormalities have been found to correlate with disease severity,[42] cortical or subcortical atrophy,[41,43] and elevated levels of serum neurofilament light chain (NfL), a neuronal cytoplasmic protein marker of axonal damage,[43] that is also sensitive to HD progression.[44,45]

The primary objective of this study was to assess whether SANDI indices were sensitive and specific to microstructural grey matter differences in the basal ganglia, compared with the thalami, in a group of individuals with premanifest and manifest HD relative to healthy controls. Secondary objectives were the exploration of the extent to which any HD-related

SANDI differences accounted for basal ganglia atrophy, assessed with volumetric measurements, and performance differences in motor tasks, including speeded and paced finger tapping, known to be associated with striatal atrophy in HD. [49]

Materials and methods

Participants

MRI data from 56 individuals who tested gene-positive for the mutant *huntingtin* allele and 57 healthy age- and sex-matched individuals (healthy controls; HC) were included in the analyses. Thirty-eight of the gene-positive individuals participated in a randomised controlled feasibility trial of HD-DRUM,[56] a remote rhythmic training intervention, with ethical approval from the Wales Research Ethics Committee 2 (REC Reference: 22/WA/0147).[55] Here we report baseline MRI and behavioural data collected prior to randomisation into the trial arms. Additionally, we included MRI data from 18 gene-positive individuals and 18 age-matched HC from a previous study characterising white matter microstructure in premanifest HD (REC Reference: 18/WA/0172).[57] Further, MRI data from 25 age- and sex-matched HC from the Wales Advanced Neuroimaging Database (WAND) Study[58] (REC Reference: 18.08.14.5332RA3) and 14 from the HD-DRUM study were utilised as comparison control. All participants provided written informed consent according to the Declaration of Helsinki prior to taking part in the studies.

HD gene-positive individuals were identified and screened for eligibility in five HD clinics in the UK (Bristol, Birmingham, Cardiff, Exeter, and Liverpool). HC volunteers were recruited from online advertisements on the Cardiff University social network, Viva Engage, or in HD clinics as support partners or family members of individuals with HD. HC participants were also recruited through Healthwise Wales and by word of mouth. For the WAND study, data collection is reported elsewhere.[58]

Individuals over the age of 18 years with a good command of the English language were eligible to participate. Additional inclusion criteria for individuals with HD[56] were:

- Positive for the presence of the mutant huntingtin allele (CAG length ≥ 36 repeats).

- Unified Huntington's Disease Rating Scale (UHDRS) Total Functional Capacity (TFC) score between 9 and 13.[59]

Exclusion criteria were:

- Contra-indication for MRI (e.g. pacemakers, stents).
- An inability to provide informed consent.
- For HD participants: A history of any other neurological condition.
- For HC: A history of any neurological or psychiatric condition, and/or alcohol or drug abuse, that have been associated with grey matter volume loss

To characterise general cognitive functioning HD participants were assessed with the Montreal Cognitive Assessment (MOCA).[61] Verbal intellectual ability was assessed with the Test of Premorbid Functioning (TOPF).[62] Disease burden for HD participants was assessed with the Total Functional Capacity (TFC) and Total Motor Score (TMS) from the United Huntington's Disease Rating Scale (UHDRS)[59] as well as their CAG repeat length and CAG-Age Product (CAP_{100}) score[63], a disease progression marker, that was calculated using the following formula:

$$CAP_{100} = Age * \frac{CAG-30}{6.49}$$

Motor outcome measures

Participants of the HD-DRUM study completed a range of motor tasks from the Quantitative-Motor (Q-Motor) test-battery,[49] which has been shown to provide reliable assessments of speeded finger tapping performance in clinical HD trials.[53,54] Tasks included left and right 1) speeded index finger tapping using force transducers,[49] 2) speeded foot tapping, 3) paced finger tapping[49] and 4) paced foot tapping with a metronome-paced and memory-paced phase, using a fast (0.55s inter-onset interval; IOI) or slow (1.1s IOI) metronome pace as well as 5) 3D pointing to four target locations in a predefined sequence using a position-tracking stylus with the dominant hand[64] and 6) 3D target pointing and speeded finger tapping dual task performed with dominant and non-dominant hand, respectively. Outcome measures for the various tasks were as follows:

- Speeded tapping: mean IOI in seconds and mean area under the curve (AUC) in Newton-seconds.

- Paced tapping: mean absolute deviation from the metronome rhythm, measured in seconds.
- Target pointing task: target frequency in Hertz (Hz).
- Target pointing-speeded tapping dual task: target frequency in Hz, mean IOI in seconds, and mean AUC in Newton-seconds.

Image acquisition

MRI data were acquired on a 3T Siemens Connectom scanner (Siemens Healthcare, Erlangen, Germany) with ultra-strong magnetic gradients (300mT/m) at Cardiff University Brain Research Imaging Centre (CUBRIC).

T1-weighted (T1w) images were acquired using a magnetisation-prepared 180-degrees radio-frequency pulses and rapid gradient-echo (MPRAGE), with the following parameters: repetition time (TR) 2,300 ms, echo time (TE) 2 ms, field of view (FOV) 256 x 256 x 192 mm, matrix size 256 x 256 x 192, resolution 1 x 1 x 1 mm^3, flip angle 9°, inversion time (TI) 857 ms, in-plane acceleration (GeneRalised Autocalibrating Partial Parallel Acquisition; GRAPPA) factor 2, phase-encoding direction anterior to posterior (AP), and acquisition time of 6 minutes.

Multi-shell High Angular Resolution Diffusion Imaging (HARDI)[65] data were obtained at b-values of 200 s/mm^2 (20 directions), 500 s/mm^2 (20 directions), 1,200 s/mm^2 (30 directions). 2,400 s/mm^2 (61 directions), 4,000 s/mm^2 (61 directions) and 6,000 s/mm^2 (61 directions) using a single-shot spin-echo, echo-planar imaging sequence with TR = 3,000 ms, TE = 59 ms, FOV 220 x 200 mm in-plane; matrix size 110 x 110 x 66; 2 mm^3 resolution, gradient pulse duration - δ = 7 ms, gradient pulses separation - Δ = 24 ms in AP phase-encoding direction with an in-plane acceleration (GRAPPA) factor of 2. Fifteen non-diffusion-weighted (b-value = 0 s/mm^2) images were acquired [two initial and 11 interspersed at the 33rd volume and every 20th volume thereafter in AP direction and 2 images in the posterior-to-anterior (PA) direction]. The HARDI acquisition time was 18 minutes.

Image processing

Diffusion-weighted image preprocessing

Multi-shell HARDI data were pre-processed and corrected for signal drift, susceptibility-induced distortions, motion and eddy current-induced distortions, gradient non-

uniformity and Gibbs ringing artifacts using a custom in-house pipeline comprising tools from the FMRIB Software Library (FSL version 6.0.3),[66] the MRtrix software package,[67] ExploreDTI [68] (version 4.8.6) and in-house MATLAB-based scripts.[39]

The FSL brain extraction tool[66] was used to mask the first non-diffusion-weighted image from each phase-encoding direction to exclude non-brain data. The diffusion-weighted MRI volumes were fitted to temporally interspersed b0 volumes to correct for within-image intensity drift by using custom code in MATLAB R2017b (MathWorks Inc., Natick, Massachusetts, USA). Slicewise outlier detection (SOLID)[69] was applied with modified Z-score thresholds of 3.5 (lower) and 10 (upper), utilising a variance-based intensity metric. FSL's top-up tool[70,71] was used to estimate susceptibility-induced off-resonance fields from b0 images that were acquired in opposing phase-encoding directions (AP and PA) and then FSL's eddy tool[72] was used to correct eddy current-induced distortions and subject movements. Gradient non-uniformity distortions were corrected using in-house code in MATLAB R2017b. Finally, Gibbs ringing correction was performed in MRtrix3 using the local subvoxel-shifts method.[73]

For the purpose of comparing our results with the previous literature,[31] DTI was fitted with ExploreDTI using data with b-values of 500 s/mm² and 1,200 s/mm² to produce outcome maps for FA and MD, estimated with linearly weighted least squares regression.

SANDI analysis

Noise level estimation and denoising of diffusion MRI data were performed using a Marchenko-Pastur principal component analysis (MP-PCA)-based method[74–76] in MRtrix3 to generate noise maps for each subject's diffusion-weighted images. These noise maps were subsequently used to fit the SANDI model[27] to the pre-processed multi-shell diffusion data with the SANDI MATLAB Toolbox (https://github.com/palombom/SANDI-Matlab-Toolbox-Latest-Release[27] using all the default settings.

The model fitting produced maps of the intra-neurite, extracellular water and intra-soma signal fractions (f_{in}, f_{ec}, f_{is}), apparent soma size (r_s; measured in μm) and intra- and extra-neurite diffusivities (D_{in}, D_e; measured in mm^2/ms). Post-hoc sensitivity analysis of the SANDI model parameters revealed very low sensitivity to changes in D_{in}. Consequently, it was excluded from further analysis.

T1-weighted image preprocessing

The default FreeSurfer [77] (v6) *recon-all* pipeline was utilised to segment subcortical basal ganglia ROIs of the caudate, putamen, and globus pallidum as well as of the thalamus as control ROIs. ROIs were segmented from T1w images and were identified and labelled in each hemisphere.

Extraction of microstructural metrics from regions-of-interest

Median values of each microstructural index from DTI (FA, MD) and SANDI (f_{is}, f_{in}, f_{ec}, r_s, D_e) models were extracted for each ROI using FSL's *fslmaths.* ROI masks were aligned with the diffusion space using rigid transformation with FSL's *flirt*[78] before eroding the boundaries of the subcortical masks to minimise partial volume effects and then aligning all microstructural maps with the masks.

Volumetric measures for each ROI and intra-cranial volume (ICV) were extracted from FreeSurfer v6. ROI volumes were normalised for ICV. The addition of brain volumes allowed exploration of the extent to which any HD-related SANDI differences accounted for basal ganglia atrophy.

Statistical analysis

Statistical analyses were performed in JASP (v0.18.1.0)[79], R version 4.4.1 (2024-06-14)[80] in R-studio (2024.9.0.375)[81] and SPSS (v27) (IBM Corp).[82] Data normality was assessed using the Shapiro-Wilk test, with $p < 0.05$ indicating non-normal distribution. Descriptive statistics for each group were reported as percentages (%), means and standard deviations (*SD*). Medians of each microstructural index in each ROI were compared between the groups with Mann-Whitney-U tests because of lack of normality and unequal variance between groups. Effect sizes for group comparisons were therefore reported with rank biserial correlation.

Hierarchical linear regression analyses were conducted to test for microstructural SANDI predictors of the variance in volumetric measurements. Regression analyses were carried out for each ROI and each group separately. HD data were modelled by firstly accounting for age and TFC scores simultaneously. This was followed by step-wise inclusion

of the SANDI indices using an iterative forward selection and backward elimination method based on each variable's F-statistic and p-value that aimed to maximise the adjusted R^2-value while keeping only the most significant predictors. HC data were modelled in the same way except for the inclusion of TFC scores.

Principal Component Analysis (PCA) was carried out to reduce the dimensionality of HD participants' Q-Motor data and hence the number of multiple correlations with microstructural SANDI indices. PCA followed established guidelines to limit the number of extracted components in relatively small sample sizes.[83,84] First the Kaiser criterion of including all components with an eigenvalue greater than 1 was applied and the Cattell scree plot was inspected to identify the minimal number of components that accounted for most variability in the data. Each extracted component was then assessed for interpretability. PCA was conducted using orthogonal Varimax rotation of the component matrix with Kaiser normalization. Loadings that were greater than 0.5 were considered to be statistically significant.

Spearman's rho correlations were then calculated between HD participants' motor component scores and the CAP_{100} with the SANDI indices, DTI and volumetric measures in each ROI.

Multiple comparisons were corrected with Benjamini-Hochberg's method to control a false discovery rate (FDR) of 0.05[85] and applied to all statistical tests that related to the same theoretical inference.[86]

Results

Demographics

Sample characteristics, including age and sex distribution for the HD and HC groups are described in Table 1. Forty-one gene-positive individuals were at premanifest stage with a TFC score of 12 or 13 and 15 individuals at early manifest stage with a TFC between 9 and 11. No statistically significant differences were observed in age and sex in the HD and HC groups ($p>0.05$). Table 2 displays descriptive statistics for the Q-Motor measures of the HD gene-positive participants.

Imaging analysis

HD-related differences in volumetric measures

Table 3 summarises the volumetric group differences across the eight ROIs. Figure 1 illustrates the effect size maps of volumetric differences between HD and HC, as well as raincloud plots for each ROI. Mann-Whitney tests identified significantly reduced volumes in all basal ganglia ROIs in HD gene-positive compared to healthy individuals. In contrast, only a marginally significant reduction was present in the right thalamus (*FDR-p* = .048) and a non-significant reduction in the left thalamus (*FDR-p* = .063).

HD-related differences in microstructural measures

Descriptive and statistical microstructural results are shown in detail in Table 4. Figure 2 provides effect size mappings and raincloud plots of the different microstructural measures for each ROI comparing the two groups.

The SANDI measures revealed between-group differences in the basal ganglia but not thalami for apparent soma density and size, and extracellular signal fraction (Fig. 2). HD gene-positive individuals exhibited reduced apparent soma density (Fig. 2A) across all basal ganglia ROIs, while apparent soma size was elevated bilaterally in the caudate and putamen but decreased in the pallidum (Fig. 2B). Elevated extracellular signal fraction was observed in the basal ganglia (Fig. 2C), while extracellular diffusivity was higher in the putamen and pallidum

but showed no significant differences in the caudate (Fig. 2D). No differences were observed for apparent neurite density f_{in} in any of the ROIs (*FDR-p* ≥ 0.167, absolute *r* < 0.2).

Regarding the DTI measures, increased FA and MD (*FDR-p* < 0.01) were observed in the basal ganglia (Fig. 2E-F) with the exception of MD in the left pallidum (*FDR-p* = 0.854).

No differences were found in the thalami for any of the microstructural metrics.

Correlations between BG microstructure and motor performance in HD

Motor measures

PCA extracted one principal component that explained 64% of the Q-Motor data with high loadings (> 0.5 or <-0.5) from all variables (Table 5). Spearman's rho correlation between Q-motor component scores and the disease burden CAP_{100} score revealed a positive correlation (rho = 0.61, p = 0.002, n = 24), i.e., higher disease burden was associated with higher scores in the Q-Motor component reflecting slower and less accurate motor performance.

Spearman's rho correlations between Q-motor component scores and SANDI microstructural measures from all ROIs and scatter plots are displayed in Figure 3. Figure 4 displays correlations and scatter plots of the Q-Motor component with DTI and volumetric indices. Overall, negative correlations were observed between principal Q-Motor component scores and apparent soma density in the basal ganglia, apparent soma size in the pallidum, and volumetric measurements in all ROIs, reflecting that lower apparent soma density and volumes were associated with impaired motor performance, reflected as higher scores in the Q-Motor component. Conversely, positive correlations were present between Q-Motor component scores and apparent soma size, extracellular signal fraction, and extracellular diffusivity in the basal ganglia, i.e. larger apparent soma size and extracellular signal were associated with impaired motor performance (Figure 3 and 4).

Microstructural predictors of BG volumes

Hierarchical linear regression analyses of the healthy control data (Table 6, Figure 5) revealed that 17% of volumetric variation in the left caudate was accounted for by age and apparent soma density while 11% of variation in the right caudate was explained by age and extracellular diffusivity (D_e). Age accounted for 25% of volumetric differences in the left putamen, and together with D_e for 29% of differences in right putamen. Age alone explained 17% of left and 11% of right thalamic volume variation. No significant regression models were present for bilateral globus pallidum.

In contrast, regression analyses for the HD data (Table 7, Figures 6 & 7) showed that 60% of volume variation in the left caudate and 51% of variation in the right caudate were accounted for by age and apparent soma density and size. Similarly, 57% of variation in the right putamen volume were explained by age and apparent soma size, while 63% of volume differences in the left putamen were explained by age, apparent soma size as well as extracellular signal and diffusivity. Comparable to the healthy control results, age alone accounted for 30% of volume variation in the left and for 35% in the right thalamus while no age effects were present for bilateral globus pallidum. However, in HD patients 42% of volume variation in the left pallidum was explained by apparent soma size and extracellular signal and 27% of volume variation in the right pallidum by extracellular signal fraction only. No significant contributions of TFC were present.

Correlation of disease burden with microstructural and volumetric measures

The CAP_{100} score as an index of disease progression was correlated with brain measurements to explore the relationship between disease burden and microstructural and volumetric differences (Figure 8). Figure 8A summarises correlation coefficient strengths and levels of significance. Figures 8B-J display scatter plots of significant correlations between the CAP_{100} and microstructural and volumetric measures. Increased CAP_{100} was negatively correlated with apparent soma density, and volume size in bilateral caudate and putamen, as well as with pallidal apparent soma size. Positive correlations were observed between CAP_{100} and extracellular diffusivity and signal fraction, apparent soma size in caudate, putamen, and

thalamus, apparent neurite density in putamen, FA in the basal ganglia, and MD in caudate and putamen.

Discussion

This is the first study to investigate HD-related microstructural differences in the basal ganglia with SANDI, a novel diffusion MRI technique, that was devised to probe grey matter microstructure. The objective of the study was to explore SANDI indices as potential non-invasive *in vivo* MRI markers of HD neuropathology that may provide more specific information about disease-related tissue abnormalities than volumetric measurements. SANDI indices of apparent soma density and size were found to be sensitive to HD pathology in the basal ganglia and explained, together with age, up to 63% of striatal atrophy in HD. Furthermore, SANDI indices correlated with motor impairments and CAP_{100} disease burden in HD. This pattern of results suggests the potential of SANDI indices for future imaging biomarkers of disease progression and of the neural effects of novel disease-modifying therapeutics in HD.

Microstructural and Volumetric Alterations in HD

Well-established patterns of significant volume loss accompanied by increases in FA and MD in the basal ganglia were replicated in HD compared with healthy controls. FA increases in the caudate and putamen are thought to occur due to the selective degeneration of medium spiny neuron connections.[20,87] No microstructural differences and only trends for volumetric reduction were present in the thalami. This pattern of macro- and microstructural differences in the basal ganglia is in accordance with previously reported changes in the basal ganglia associated with premanifest and early manifest HD stages.[32,88]

Importantly, the application of SANDI revealed novel information about HD-related microstructural differences in the basal ganglia. In HD gene-positive compared with healthy individuals, apparent soma density was reduced and accompanied by increases in extracellular water fraction and diffusivity across the caudate, putamen, and pallidum but not the thalami. This pattern of results is consistent with the loss of medium spiny neurons in the caudate and putamen, the histopathological hallmark of HD [22,23], as well as subsequent spread of neurodegeneration to the globus pallidum and other surrounding regions. Thus, the pattern of differences in apparent soma size may capture cellular processes associated with different stages of neuropathology across the midbrain. Further, apparent soma size was increased in the caudate and putamen and reduced in the globus pallidum in individuals with HD. Changes in apparent soma size may reflect shifts in the proportion of neural and glial cell density as well

as morphological changes including astrocyte and microglia swelling in response to established neurodegeneration[22,24–26] and soma shrinkage prior to neuronal cell death.[89,90]

The pattern of microstructural predictors of HD-related atrophy identified in the regression analyses may also reflect disproportionate pathological changes in the striatum with relative sparing of surrounding regions such as the thalami at early stages of the disease. Up to 63% of HD-related striatal atrophy was predicted by apparent soma density and size and age. This dropped to 27% and 42% of atrophy in right and left pallidum explained by apparent soma size and extracellular signal fraction, while age alone accounted for volume differences in the thalami. The latter finding in the thalami mirrored the pattern of results in the healthy control data where age was the most significant predictor across all ROIs (except bilateral pallidum) and the only predictor in the thalami, while diffusivity contributed to right-lateralised basal ganglia regions and apparent soma density to left caudate only.

Together these results demonstrate that SANDI indices of apparent soma density and size may capture HD-related differences in striatal grey matter microstructure *in vivo*. Striatal reductions in apparent soma density and increases in apparent soma size are in accordance with the HD characteristic loss of medium spiny neurons and reactive astrocytes and microglia and explained a significant proportion of HD-related atrophy in the caudate and the putamen.

Associations Between SANDI microstructural indices and Motor Function

The observed correlations between SANDI metrics and motor measures provide novel insights into the functional implications of microstructural alterations in HD. Consistent with the role of the basal ganglia in motor initiation and coordination,[91] the present study demonstrated that microstructural differences in HD, notably reduced apparent soma density in the striatum and reduced apparent soma size in the pallidum were associated with poorer Q-Motor performance, which in turn was associated with larger disease burden. This is evidenced by increased IOI and ACU in speeded tapping tasks, as well as difficulties in synchronising with the metronome during the metronome tapping task. Similarly, increased apparent soma size in the striatum, as well as elevated extracellular water signal, extracellular diffusivity across all three basal ganglia regions, and striatal FA and MD, were linked to motor impairments. These findings suggest that microstructural differences likely due to the loss of

striatal medium spiny neurons and associated glial reactivity are directly linked to subtle motor impairments.

Clinical Implications and Future Directions

The present study acquired multi-shell (max b-value = 6,000 s/mm^2) DWI data on a non-clinical ultra-strong gradient (300mT/m) 3T MRI system. Ultra-strong gradient imaging has the advantage of improving the signal-to-noise-ratio at high b-values due to shorter echo times (TE), which in turn provides enhanced sensitivity to small water displacement,[39] and minimises bias due to inter-compartmental exchange.[47,48] However, it is important to note that it has been demonstrated feasible to acquire multi-shell DWI data for SANDI modelling on standard clinical 3T MRI systems,[46] and that such acquisitions have been shown to be sensitive to neuropathology in MS.[43] Thus, it is possible apply SANDI indices clinically.

Our findings highlight the potential of SANDI-derived metrics as future markers for tracking disease progression and assessing therapeutic efficacy. The sensitivity of apparent soma density and size, and extracellular water signal to microstructural changes in HD offers a complementary perspective to volumetric measures, which are currently the most widely employed imaging modality in clinical trials. Furthermore, the associations between SANDI metrics and motor measures that were correlated with disease burden scores underscore their relevance in evaluating the efficacy of emerging disease-modifying treatments.

Conclusion

In our study, we demonstrate the utility of SANDI for characterising microstructural abnormalities in HD, providing a detailed view of basal ganglia pathology and its implications for motor functions. By bridging the gap between histopathological findings and *in vivo* imaging, SANDI offers a promising avenue for advancing HD research and clinical care.

Table 1. Demographic and clinical information of participants

	HD group		**HC group**		***Statistic (p-value)***
	N	Mean (SD)	*N*	Mean (SD)	
Age	*56*	46.12 (13.79)	*57*	44.96 (13.75)	$t_{(111)}$ = 0.446 (0.657)
Sex (Male/Female)		31/25		26/31	χ^2 = 1.073 (0.300)
Education (years)	*38*	14.16 (2.58)	14	15.86 (2.54)	$t_{(50)}$ = 2.06 (0.448)
MOCA	*55*	26.47 (3.55)		-	
TOPF	*56*	49.70 (13.16)		-	
UHDRS-TFC	*56*	12.11 (1.25)		-	
UHDRS-TMS	*38*	10.63 (14.19)		-	
CAG	*43*	41.56 (2.67)		-	
CAP	*43*	78.65 (22.83)		-	

Abbreviations: **CAG**: Cytosine Adenine Guanine; **CAP**: CAG-Age-Product; **HC**: Healthy controls; **HD**: Huntington's disease; **MOCA**: Montreal Cognitive Assessment; **SD**: Standard deviation; **TFC**: Total Functional Capacity; **TMS**: Total Motor Score; **TOPF**: Test of Premorbid Functioning; **UHDRS**: United Huntington's Disease Rating Scale

Table 2. Descriptive statistics for motor outcome measures

	HD group	
Task *Outcome measure*	**N**	**Mean (SD)**
Speeded tapping		
Left finger; Area under the curve (N-s)	38	0.13 (0.20)
Right finger; Area under the curve (N-s)	38	0.07 (0.09)
Left finger; Inter-onset interval (s)	38	0.26 (0.12)
Right finger; Inter-onset interval (s)	38	0.23 (0.08)
Left foot; Inter-onset interval (s)	37	0.37 (0.20)
Right foot; Inter-onset interval (s)	38	0.35 (0.18)
Metronome tapping; Absolute deviation from pace (s)		
Left finger; Paced; Fast	38	0.07 (0.06)
Left finger; Paced; Slow	38	0.13 (0.14)
Left finger; Unpaced; Fast	38	0.07 (0.07)
Left finger; Unpaced; Slow	38	0.15 (0.15)
Right finger; Paced; Fast	38	0.07 (0.06)
Right finger; Paced; Slow	38	0.13 (0.12)
Right finger; Unpaced; Fast	38	0.08 (0.06)
Right finger; Unpaced; Slow	38	0.16 (0.17)
Left foot; Paced; Fast	36	0.07 (0.05)
Left foot; Paced; Slow	35	0.16 (0.13)
Left foot; Unpaced; Fast	36	0.08 (0.09)
Left foot; Unpaced; Slow	35	0.17 (0.14)
Right foot; Paced; Fast	37	0.08 (0.04)
Right foot; Paced; Slow	37	0.16 (0.12)
Right foot; Unpaced; Fast	37	0.09 (0.09)
Right foot; Unpaced; Slow	37	0.16 (0.13)
Pointing (dominant hand)		
Target frequency over trial (Hz)	38	2.62 (0.65)
Pointing (dominant) and tapping (non-dominant)		
Finger tapping area under the curve (coefficient of variation %)	38	0.76 (0.37)
Finger tapping area under the curve (N-s)	38	0.31 (0.43)
Finger tapping inter-onset interval (s)	38	0.39 (0.19)
Frequency over trial (Hz)	38	3.08 (1.07)
Pointing target frequency over trial (Hz)	38	2.62 (0.66)

Abbreviations: Hz: Hertz; **N:** Newton; **s:** seconds

Table 3. Descriptive and Mann-Whitney Statistics for Intracranial Volume-Normalised Regions of Interest

		HD group	**HC group**	**Statistic (FDR-p, effect size)**
Region of interest	**L/R**	**Mean (SD)**	**Mean (SD)**	**U (p, rank-biserial correlation)**
Caudate	*L*	1.95[a] (0.45[a])	2.35[a] (0.24[a])	**2464 (<0.001, 0.544)**
	R	2.06[a] (0.43[a])	2.41[a] (0.25[a])	**2376 (<0.001, 0.489)**
Putamen	*L*	2.67[a] (0.62[a])	3.22[a] (0.46[a])	**2397 (<0.001, 0.502)**
	R	2.67[a] (0.66[a])	3.25[a] (0.40[a])	**2479 (<0.001, 0.553)**
Pallidum	*L*	1.15[a] (0.20[a])	1.32[a] (0.13[a])	**2382 (<0.001, 0.492)**
	R	1.13[a] (0.17[a])	1.26[a] (0.12[b])	**2323 (<0.001, 0.456)**
Thalamus	*L*	4.83[a] (0.49[a])	4.99[a] (0.41[b])	1955 (0.063, 0.224)
	R	4.72[a] (0.39[a])	4.91[a] (0.40[b])	**1981 (0.048, 0.241)**

Abbreviations: **FDR**: False discovery rate; **HC**: Healthy controls; **HD**: Huntington's disease; **L**: Left hemisphere; **R**: Right hemisphere; **SD**: Standard deviation

[a]: multiplied by 10^{-3}

Table 4. Descriptive and Mann-Whitney Statistics for Microstructural Measures in Regions of Interest

			HD group	**HC group**	**Statistic (FDR-p, effect size)**
Microstructural measure	**Region of interest**	**L/R**	**Mean (SD)**	**Mean (SD)**	***U* (*p, rank-biserial correlation*)**
Apparent soma density	*Caudate*	*L*	0.43 (0.05)	0.46 (0.02)	**2227 (<0.001, 0.395)**
		R	0.45 (0.05)	0.48 (0.02)	**2318 (<0.001, 0.452)**
	Putamen	*L*	0.39 (0.05)	0.42 (0.03)	**2140 (0.003, 0.341)**
		R	0.42 (0.05)	0.44 (0.03)	**2099 (0.007, 0.315)**
	Pallidum	*L*	0.21 (0.05)	0.24 (0.04)	**2187 (0.001, 0.370)**
		R	0.21 (0.05)	0.24 (0.04)	**2249 (<0.001, 0.409)**
	Thalamus	*L*	0.34 (0.03)	0.34 (0.02)	1692 (0.701, 0.060)
		R	0.35 (0.03)	0.35 (0.02)	1661 (0.776, 0.041)
Apparent soma size	*Caudate*	*L*	9.80 (0.25)	9.58 (0.15)	**746 (<0.001, -0.533)**
		R	9.72 (0.25)	9.52 (0.12)	**751 (<0.001, -0.529)**
	Putamen	*L*	9.61 (0.29)	9.43 (0.15)	**885 (<0.001, -0.445)**
		R	9.63 (0.27)	9.40 (0.14)	**791 (<0.001, -0.504)**
	Pallidum	*L*	8.41 (1.08)	8.88 (0.58)	**2126 (0.004, 0.332)**
		R	8.59 (0.94)	9.05 (0.45)	**2300 (<0.001, 0.447)**
	Thalamus	*L*	9.51 (0.14)	9.50 (1.32)	1502 (0.701, -0.059)
		R	9.54 (0.13)	9.52 (0.12)	1515 (0.723, -0.051)
Extracellular water signal fraction	*Caudate*	*L*	0.38 (0.04)	0.36 (0.01)	**757 (<0.001, -0.526)**
		R	0.37 (0.02)	0.36 (0.01)	**984 (<0.001, -0.383)**
	Putamen	*L*	0.36 (0.03)	0.34 (0.02)	**1048 (0.003, -0.343)**
		R	0.34 (0.03)	0.32 (0.01)	**892 (<0.001, -0.441)**
	Pallidum	*L*	0.36 (0.04)	0.33 (0.02)	**910 (<0.001, -0.430)**
		R	0.35 (0.04)	0.32 (0.02)	**932 (<0.001, -0.416)**
	Thalamus	*L*	0.34 (0.02)	0.33 (0.01)	1294 (0.130, -0.189)
		R	0.33 (0.01)	0.32 (0.01)	1636 (0.853, 0.025)
Extracellular diffusivity	*Caudate*	*L*	1.47 (0.28)	1.40 (0.11)	1420 (0.418, -0.110)
		R	1.51 (0.25)	1.44 (0.13)	1482 (0.633, -0.071)
	Putamen	*L*	1.47 (0.17)	1.36 (0.11)	**902 (<0.001, -0.435)**
		R	1.62 (0.20)	1.49 (0.11)	**1002 (0.001, -0.372)**
	Pallidum	*L*	1.62 (0.20)	1.48 (0.12)	**842 (<0.001, -0.472)**
		R	1.76 (0.23)	1.59 (0.14)	**809 (<0.001, -0.493)**
	Thalamus	*L*	1.47 (0.07)	1.44 (0.07)	1411 (0.394, -0.116)
		R	0.31 (0.03)	0.31 (0.03)	1377 (0.305, -0.137)
Apparent neurite density	*Caudate*	*L*	0.18 (0.04)	0.17 (0.02)	1514 (0.723, -0.051)
		R	0.18 (0.05)	0.16 (0.02)	1317 (0.167, -0.175)
	Putamen	*L*	0.24 (0.04)	0.23 (0.03)	1374 (0.303, -0.139)
		R	0.23 (0.04)	0.23 (0.03)	1411 (0.394, -0.116)
	Pallidum	*L*	0.41 (0.05)	0.42 (0.03)	1553 (0.854, -0.027)
		R	0.43 (0.05)	0.43 (0.03)	1473 (0.605, -0.078)
	Thalamus	*L*	0.31 (0.03)	0.31 (0.03)	1565 (0.868, -0.019)
		R	0.31 (0.03)	0.31 (0.03)	1459 (0.554, -0.086)
Fractional anisotropy	*Caudate*	*L*	0.18 (0.04)	0.16 (0.02)	**993 (0.001, -0.378)**

		R	0.20 (0.07)	0.16 (0.02)	**889 (<0.001, -0.443)**
	Putamen	*L*	0.19 (0.04)	0.17 (0.02)	**873 (<0.001, -0.453)**
		R	0.20 (0.04)	0.17 (0.02)	**710 (<0.001, -0.555)**
	Pallidum	*L*	0.28 (0.04)	0.26 (0.03)	**1115 (0.010, -0.301)**
		R	0.28 (0.05)	0.26 (0.02)	**995.5 (<0.001, -0.401)**
	Thalamus	*L*	0.33 (0.02)	0.33 (0.02)	1808 (0.319, 0.133)
		R	0.33 (0.02)	0.33 (0.02)	1532 (0.776, -0.040)
Mean diffusivity	*Caudate*	*L*	6.50[a] (0.41[a])	6.23[a] (0.13[a])	**777.5 (<0.001, -0.513)**
		R	6.44[a] (0.36[a])	6.20[a] (0.12[a])	**760.5 (<0.001, -0.523)**
	Putamen	*L*	6.22[a] (0.34[a])	5.95[a] (0.15[a])	**653.5 (<0.001, -0.591)**
		R	6.20[a] (0.34[a])	5.91[a] (0.13[a])	**624.5 (<0.001, -0.609)**
	Pallidum	*L*	5.54[a] (0.36[a])	5.51[a] (0.23[a])	1557.5 (0.854, -0.024)
		R	5.52[a] (0.30[a])	5.49[a] (0.18[a])	1437 (0.474, -0.100)
	Thalamus	*L*	5.98[a] (0.14[a])	5.96[a] (0.11[a])	1509 (0.721, -0.055)
		R	6.01[a] (0.13[a])	6.00[a] (0.11[a])	1566.5 (0.868, -0.018)

Abbreviations: **FDR**: False discovery rate; **HC**: Healthy controls; **HD**: Huntington's disease; **L**: Left hemisphere; **R**: Right hemisphere; **SD**: Standard deviation

[a]: multiplied by 10^{-4}

Table 5. Rotated Component Loadings on the Q-motor Outcome Measures

Task *Outcome measure*	**Q-motor Factor**
Speeded tapping	
Left finger; Area under the curve (N-s)	**0.707**
Right finger; Area under the curve (N-s)	**0.723**
Left finger; Inter-onset interval (s)	**0.772**
Right finger; Inter-onset interval (s)	**0.859**
Left foot; Inter-onset interval (s)	**0.798**
Right foot; Inter-onset interval (s)	**0.893**
Metronome tapping; Absolute deviation from pace (s)	
Left finger; Paced; Fast	**0.875**
Left finger; Paced; Slow	**0.832**
Left finger; Unpaced; Fast	**0.936**
Left finger; Unpaced; Slow	**0.913**
Right finger; Paced; Fast	**0.730**
Right finger; Paced; Slow	**0.672**
Right finger; Unpaced; Fast	**0.886**
Right finger; Unpaced; Slow	**0.865**
Left foot; Paced; Fast	**0.823**
Left foot; Paced; Slow	**0.883**
Left foot; Unpaced; Fast	**0.884**
Left foot; Unpaced; Slow	**0.900**
Right foot; Paced; Fast	**0.818**

Right foot; Paced; Slow	**0.885**
Right foot; Unpaced; Fast	**0.890**
Right foot; Unpaced; Slow	**0.740**
Pointing (dominant hand)	
Target frequency over trial (Hz)	**-0.525**
Pointing (dominant) and tapping (non-dominant)	
Finger tapping area under the curve (N-s)	**0.734**
Finger tapping inter-onset interval (s)	**0.788**
Frequency over trial (Hz)	**-0.756**
Pointing target frequency over trial (Hz)	**-0.568**

All loadings were significant (>0.5 and < -0.5) and are highlighted in bold.

Abbreviations: Hz: Hertz; **N:** Newton; **s:** seconds

Table 6. Hierarchical Linear Regression Predicting Normalised Volumes from SANDI Microstructural Metrics, Controlling for Age in the Healthy Control Participants

ROI	Model	Predictor(s)	*Adjusted R^2*	*ΔR^2*	*F-value (p-value)*	*ΔF-value*	*β*	*t-value*	*p-value*
Left Caudate	1	Age	0.084	0.100	**6.115 (0.017)**		-0.316	-2.473	**0.031**
	2	Age	0.167	0.096	**6.599 (0.003)**	6.474	-0.166	-1.226	0.297
		f_{is}					0.345	2.544	**0.026**
Left Putamen	1	Age	0.247	0.260	**19.328 (<0.001)**		-0.510	- 4.396	**<0.001**
Left Pallidum	1	Age	0.004	0.022	1.247 (0.269)		-0.149	-1.117	0.341
Left Thalamus	1	Age	0.174	0.188	**12.761 (0.001)**		-0.434	-3.572	**0.003**
Right Caudate	1	Age	0.046	0.063	3.715 (0.059)		-0.252	-1.927	0.087
	2	Age	0.111	0.080	**4.508 (0.015)**	5.029	-0.348	-2.616	**0.023**
		D_e					0.299	2.243	**0.048**
Right Putamen	1	Age	0.234	0.248	**18.109 (<0.001)**		-0.498	-4.255	**<0.001**
	2	Age	0.289	0.067	**12.389 (<0.001)**	5.265	-0.602	-4.954	**<0.001**
		De					0.279	2.295	**0.045**
Right Pallidum	1	Age	-0.017	0.001	.058 (0.811)		0.032	0.241	0.847
	2	Age	0.108	0.139	**4.392 (0.017)**	8.718	0.003	0.025	0.980
		D_e					0.374	2.953	**0.011**
Right Thalamus	1	Age	0.111	0.127	**7.966 (0.007)**		-0.356	-2.822	**0.015**

Model 1: Volume(ROI)=$\beta_0+\beta_1$*(Age) +ϵ; **Model 2-n**: Volume (ROI)=$\beta_0+\beta_1$*(Age)+ $\beta_{2\text{-}n}$*(f_{is}, r_s, f_{ec}, D_e, f_{in})+ϵ; Predictors in Model 1 were entered simultaneously; predictors in Models 2-n were entered in a stepwise fashion using an iterative forward selection and backward elimination method to maximise the adjusted R^2while keeping only the most significant predictors.

Abbreviations: De: Extracellular diffusivity; **fec:** Extracellular water signal fraction; **fin:** Neurite density signal fraction; **fis:** Soma density signal fraction; **rs:** Soma size; **SANDI:** Soma and Neurite Density Imaging; **TFC:** Total functional capacity

Significant F-values and t-values are highlighted in **bold**

Table 7. Hierarchical Linear Regression Models Predicting Normalised Volumes in each Region of Interest from SANDI Microstructural Metrics, Controlling for Age and TFC in HD Gene-Positive Participants

ROI	Model	Predictors	*Adjusted R^2*	*ΔR^2*	*F-value (p-value)*	*ΔF-value*	*β*	*t-value*	*p-value*
Left Caudate	1	Age	0.277	0.304	**11.136 (<0.001)**		-0.398	-3.249	**0.005**
		TFC					0.280	2.281	**0.046**
	2	Age	0.547	0.268	**22.308 (<0.001)**	31.383	-0.370	-3.810	**<0.001**
		TFC					-0.034	-0.303	0.822
		r_s					-0.611	-5.602	**<0.001**
	3	Age	0.600	0.058	**20.853 (<0.001)**	7.623	-0.273	-2.788	**0.016**
		TFC					-0.068	-0.638	0.594
		r_s					-0.529	-4.963	**<0.001**
		f_{is}					0.288	2.761	**0.016**
Left Putamen	1	Age	0.296	0.323	**12.150 (<0.001)**		-0.415	-3.436	**0.003**
		TFC					0.282	2.331	**0.043**
	2	Age	0.529	0.233	**20.855 (<0.001)**	26.238	-0.332	-3.311	**0.005**
		TFC					0.173	1.711	0.129
		f_{ec}					-0.507	-5.122	**<0.001**
	3	Age	0.601	0.075	**20.934 (<0.001)**	9.961	-0.341	-3.690	**0.003**
		TFC					0.071	0.721	0.552
		f_{ec}					-0.427	-4.515	**<0.001**
		r_s					-0.309	-3.156	**0.007**
	4	Age	0.630	0.034	**19.016 (<0.001)**	4.818	-0.485	-4.386	**<0.001**
		TFC					0.168	1.605	0.157
		f_{ec}					-0.489	-5.126	**<0.001**
		r_s					-0.349	-3.638	**0.003**
		D_e					0.302	2.195	0.052
Left Pallidum	1	Age	0.107	0.140	**4.165 (0.021)**		-0.152	-1.119	0.341
		TFC					0.299	2.198	0.052
	2	Age	0.344	0.241	**10.278 (<0.001)**	19.485	0.035	0.278	0.829
		TFC					0.111	0.889	0.455
		f_{ec}					-0.577	-4.414	**<0.001**
	3	Age	0.424	0.086	**10.741 (<0.001)**	7.885	0.115	0.961	0.425
		TFC					0.049	0.417	0.753
		f_{ec}					-0.486	-3.837	**0.001**
		r_s					0.344	2.808	**0.015**
Left Thalamus	1	Age	0.302	0.328	**12.455 (<0.001)**		-0.456	-3.786	**0.001**
		TFC					0.236	1.956	0.085
Right Caudate	1	Age	0.276	0.304	**11.117 (<0.001)**		-0.410	-3.341	**0.005**
		TFC					0.265	2.162	0.054
	2	Age	0.443	0.171	**15.036 (<0.001)**	16.233	-0.426	-3.957	**0.001**
		TFC					0.006	0.048	0.976
		r_s					-0.485	-4.029	**0.001**
	3	Age	0.510	0.073	**14.807 (<0.001)**	7.898	-0.326	-3.043	**0.009**
		TFC					-0.018	-0.156	0.902
		r_s					-0.456	-4.020	**0.001**
		f_{is}					0.296	2.810	**0.015**
Right Putamen	1	Age	0.333	0.358	**14.218 (<0.001)**		-0.499	-4.243	**<0.001**

		TFC					0.211	1.797	0.111
	2	Age	0.570	0.236	**24.432 (<0.001)**	29.159	-0.425	-4.450	**<0.001**
		TFC					-0.070	-0.652	0.593
		rs					-0.578	-5.400	**<0.001**
Right Pallidum	1	Age	0.043	0.079	2.177 (0.124)		-0.043	-0.308	0.822
		TFC					0.264	1.874	0.097
	2	Age	0.265	0.228	**7.367 (<0.001)**	16.430	0.094	0.737	0.550
		TFC					0.116	0.902	0.454
		f_{ec}					-0.530	-4.053	**0.001**
Right Thalamus	1	Age	0.347	0.372	**15.076 (<0.001)**		-0.550	-4.723	**<0.001**
		TFC					0.145	1.242	0.295

Model 1: Volume(ROI)=$\beta_0+\beta_1$*(Age)+β_2*(TFC) +ϵ; **Model 2-n**: Volume (ROI)=$\beta_0+\beta_1$*(Age)+β_2*(TFC)+$\beta_{3\text{-}n}$*(f_{is}, r_s, f_{ec}, D_e, f_{in})+ϵ; Predictors in Model 1 were entered simultaneously; predictors in Models 2-n were entered in a stepwise fashion using an iterative forward selection and backward elimination method to maximise the adjusted R^2while keeping only the most significant predictors.

Abbreviations: De: Extracellular diffusivity; **fec:** Extracellular water signal fraction; **fin:** Neurite density signal fraction; **fis:** Soma density signal fraction; **HD:** Huntington's disease; **rs:** Soma size; **SANDI:** Soma and Neurite Density Imaging; **TFC:** Total functional capacity

Significant F-values and t-values ($p<0.05$) are highlighted in **bold**

Figures

Figure 1

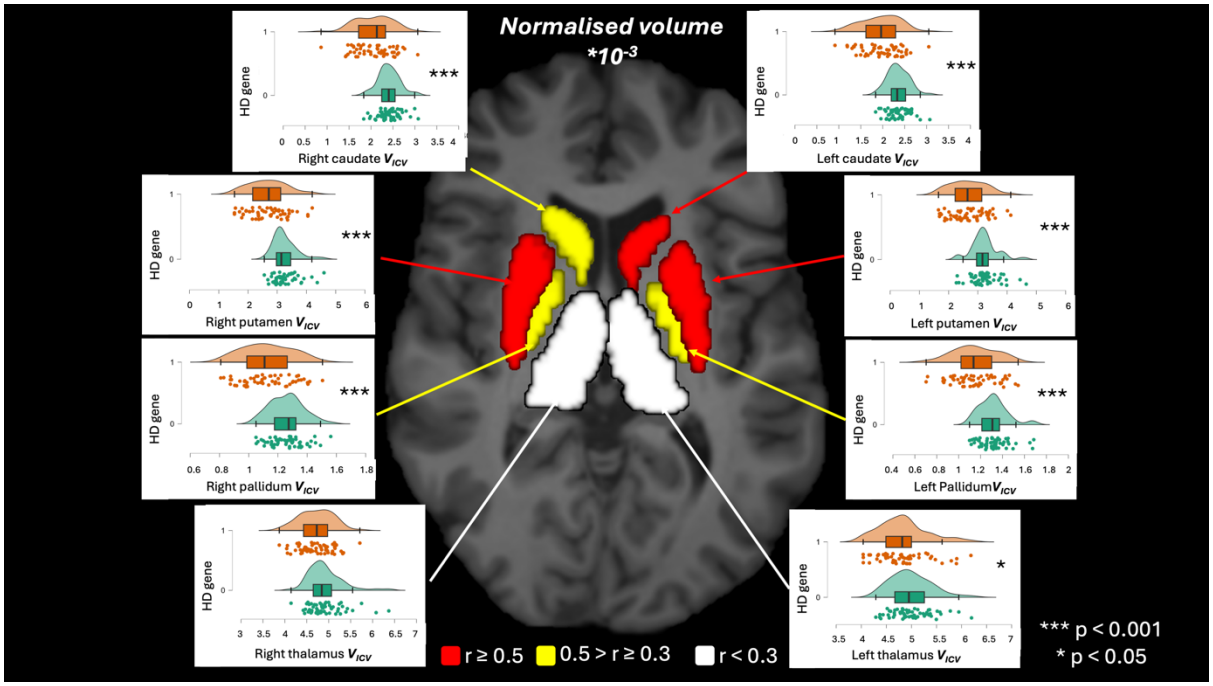

Figure 2

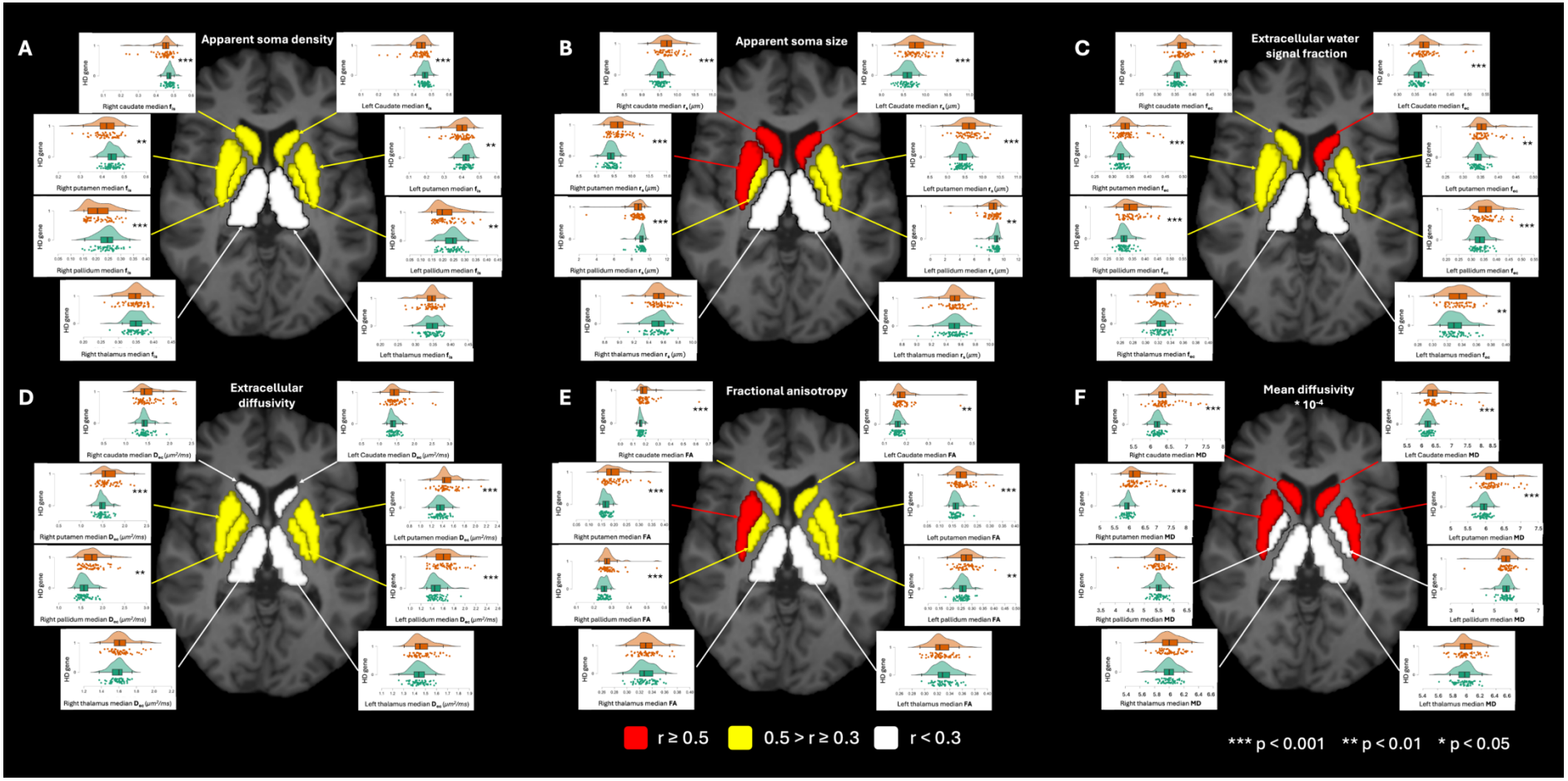
A
Apparent soma density
B
Apparent soma size
C
Extracellular water signal fraction
D
Extracellular diffusivity
E
Fractional anisotropy
F
Mean diffusivity * 10-4
r ≥ 0.5
0.5 > r ≥ 0.3
r < 0.3
*** p < 0.001
** p < 0.01
* p < 0.05

Figure 3

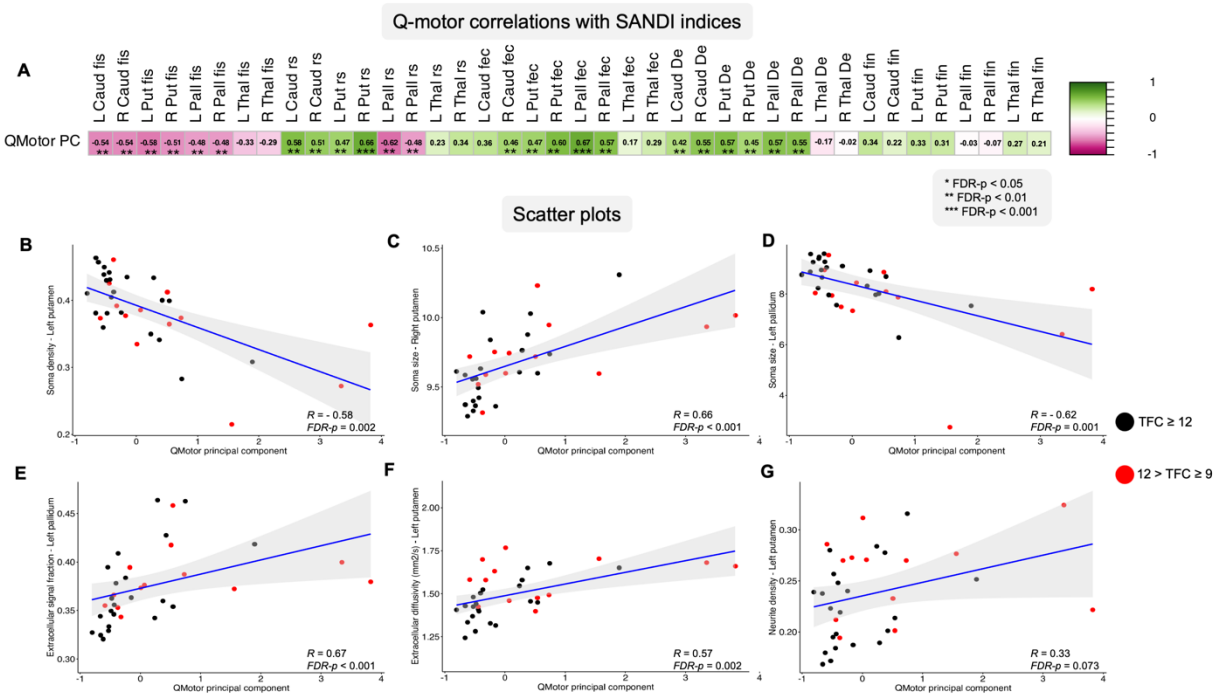
Q-motor correlations with SANDI indices
A
L Caud fis
R Caud fis
L Put fis
R Put fis
L Pall fis
R Pall fis
L Thal fis
R Thal fis
L Caud rs
R Caud rs
L Put rs
R Put rs
L Pall rs
R Pall rs
L Thal rs
R Thal rs
L Caud fec
R Caud fec
L Put fec
R Put fec
L Pall fec
R Pall fec
L Thal fec
R Thal fec
L Caud De
R Caud De
L Put De
R Put De
L Pall De
R Pall De
L Thal De
R Thal De
L Caud fin
R Caud fin
L Put fin
R Put fin
L Pall fin
R Pall fin
L Thal fin
R Thal fin
QMotor PC
-0.54 -0.54 -0.58 -0.51 -0.48 -0.48 -0.33 -0.29 0.58 0.51 0.47 0.66 -0.62 -0.48 0.23 0.34 0.36 0.46 0.47 0.60 0.67 0.57 0.17 0.29 0.42 0.55 0.57 0.45 0.57 0.55 -0.17 -0.02 0.34 0.22 0.33 0.31 -0.03 -0.07 0.27 0.21
1
0
-1
* FDR-p < 0.05
** FDR-p < 0.01
*** FDR-p < 0.001
Scatter plots
B
Soma density - Left putamen
R = - 0.58
FDR-p = 0.002
QMotor principal component
C
Soma size - Right putamen
R = 0.66
FDR-p < 0.001
QMotor principal component
D
Soma size - Left pallidum
R = - 0.62
FDR-p = 0.001
QMotor principal component
TFC ≥ 12
12 > TFC ≥ 9
E
Extracellular signal fraction - Left pallidum
R = 0.67
FDR-p < 0.001
QMotor principal component
F
Extracellular diffusivity (mm2/s) - Left putamen
R = 0.57
FDR-p = 0.002
QMotor principal component
G
Neurite density - Left putamen
R = 0.33
FDR-p = 0.073
QMotor principal component

Figure 4

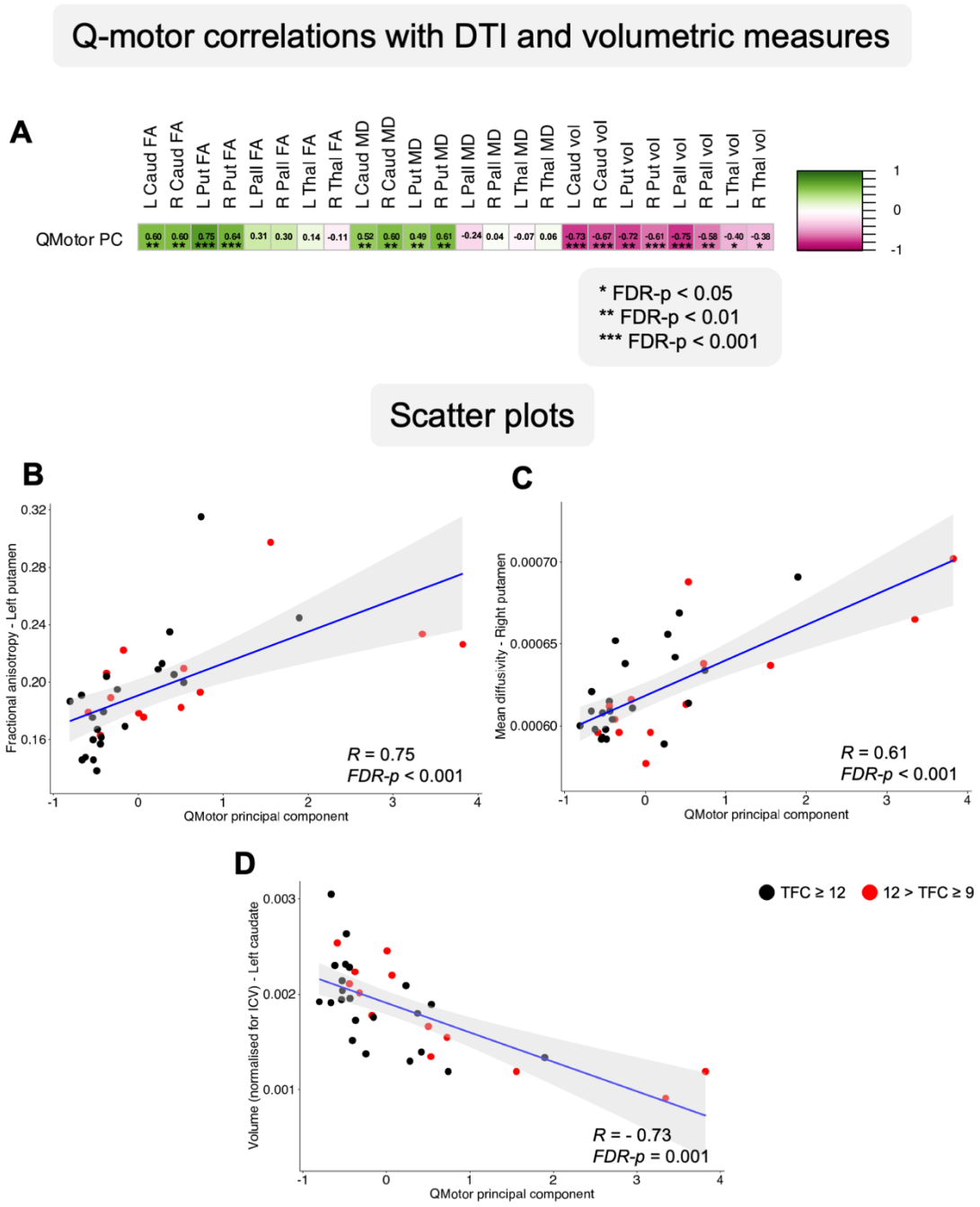
Q-motor correlations with DTI and volumetric measures
A
L Caud FA
R Caud FA
L Put FA
R Put FA
L Pall FA
R Pall FA
L Thal FA
R Thal FA
L Caud MD
R Caud MD
L Put MD
R Put MD
L Pall MD
R Pall MD
L Thal MD
R Thal MD
L Caud vol
R Caud vol
L Put vol
R Put vol
L Pall vol
R Pall vol
L Thal vol
R Thal vol
QMotor PC
0.60 **
0.60 **
0.75 ***
0.64 ***
0.31
0.30
0.14
-0.11
0.52 **
0.60 **
0.49 **
0.61 **
-0.24
0.04
-0.07
0.06
-0.73 ***
-0.67 ***
-0.72 **
-0.61 ***
-0.75 ***
-0.58 **
-0.40 *
-0.38 *
1
0
-1
* FDR-p < 0.05
** FDR-p < 0.01
*** FDR-p < 0.001
Scatter plots
B
Fractional anisotropy - Left putamen
QMotor principal component
R = 0.75
FDR-p < 0.001
C
Mean diffusivity - Right putamen
QMotor principal component
R = 0.61
FDR-p < 0.001
D
Volume (normalised for ICV) - Left caudate
QMotor principal component
R = - 0.73
FDR-p = 0.001
TFC ≥ 12
12 > TFC ≥ 9

Figure 5

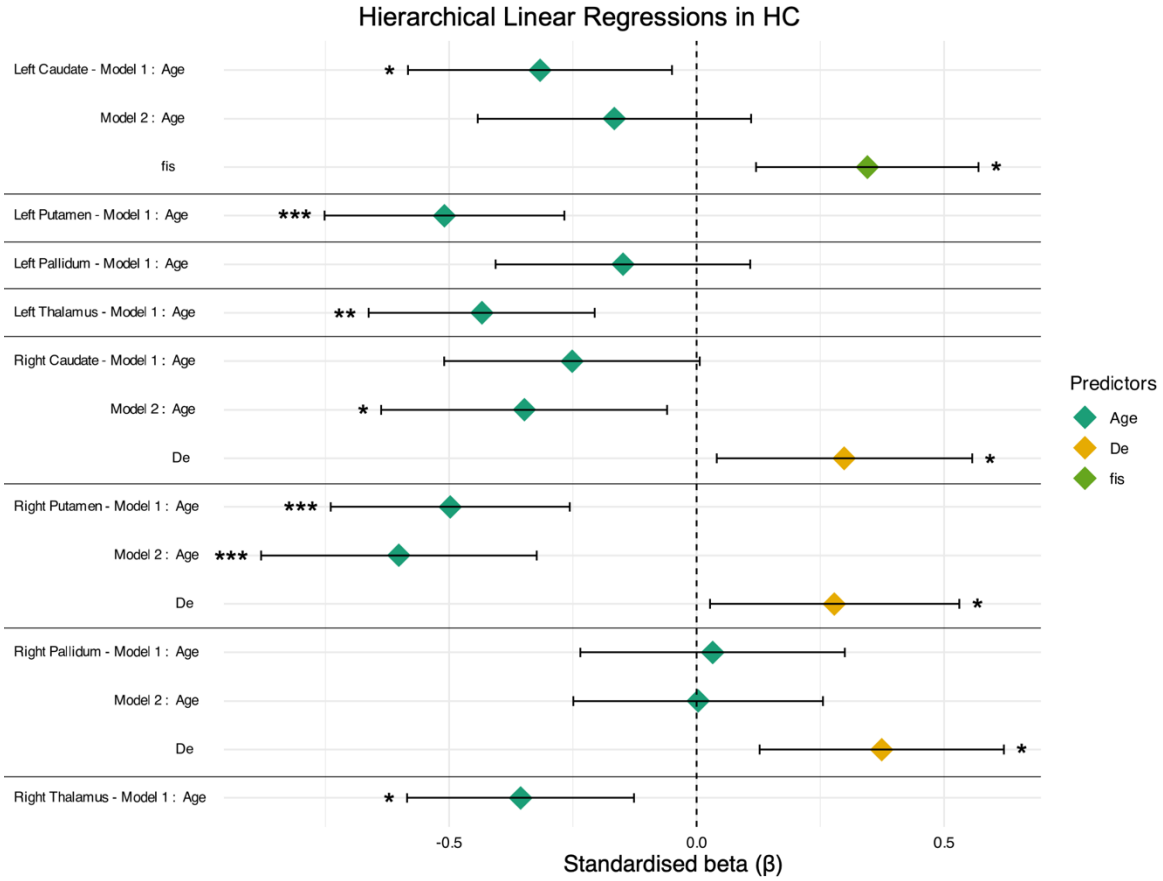
Hierarchical Linear Regressions in HC
Left Caudate - Model 1 : Age
Model 2 : Age
fis
Left Putamen - Model 1 : Age
Left Pallidum - Model 1 : Age
Left Thalamus - Model 1 : Age
Right Caudate - Model 1 : Age
Model 2 : Age
De
Right Putamen - Model 1 : Age
Model 2 : Age
De
Right Pallidum - Model 1 : Age
Model 2 : Age
De
Right Thalamus - Model 1 : Age
-0.5
0.0
0.5
Standardised beta (β)
Predictors
Age
De
fis

Figure 6

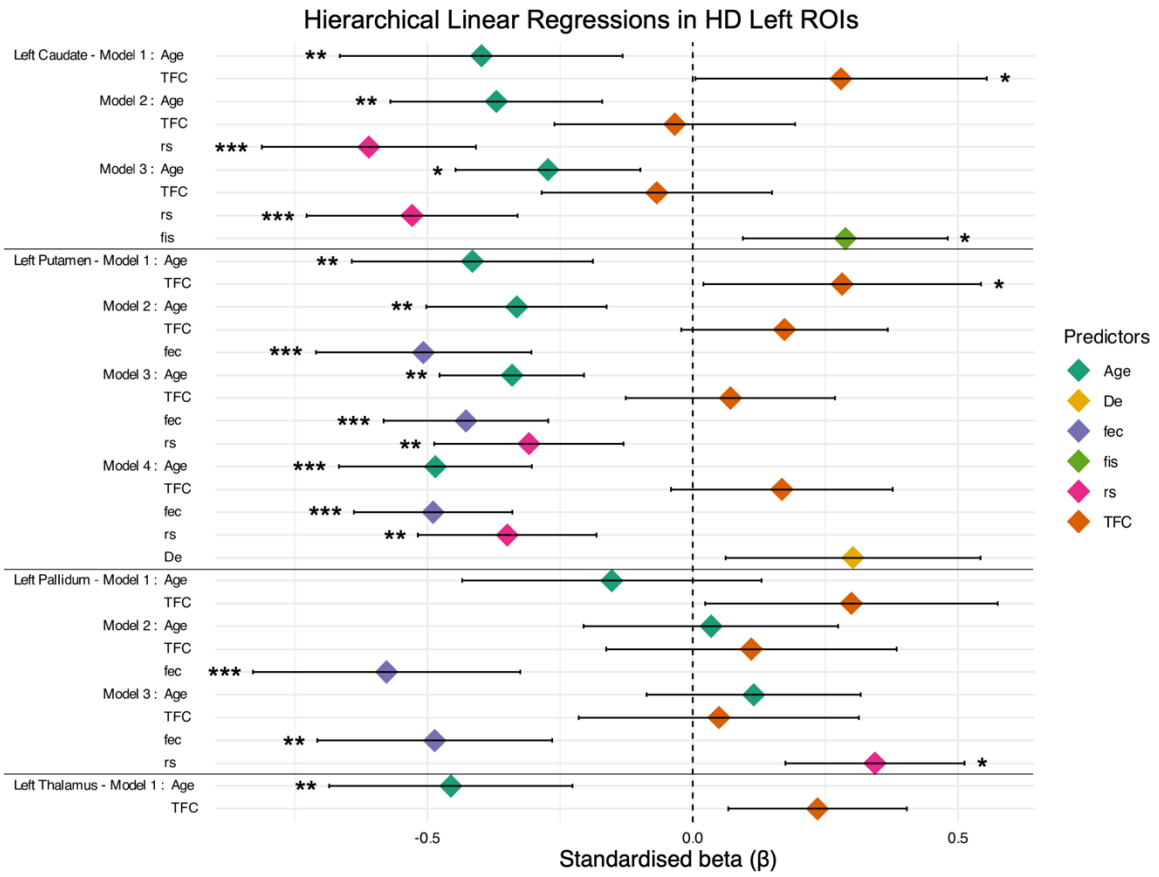
Hierarchical Linear Regressions in HD Left ROIs
Left Caudate - Model 1 : Age
TFC
Model 2 : Age
TFC
rs
Model 3 : Age
TFC
rs
fis
Left Putamen - Model 1 : Age
TFC
Model 2 : Age
TFC
fec
Model 3 : Age
TFC
fec
rs
Model 4 : Age
TFC
fec
rs
De
Left Pallidum - Model 1 : Age
TFC
Model 2 : Age
TFC
fec
Model 3 : Age
TFC
fec
rs
Left Thalamus - Model 1 : Age
TFC
-0.5
0.0
0.5
Standardised beta (β)
Predictors
Age
De
fec
fis
rs
TFC

Figure 7

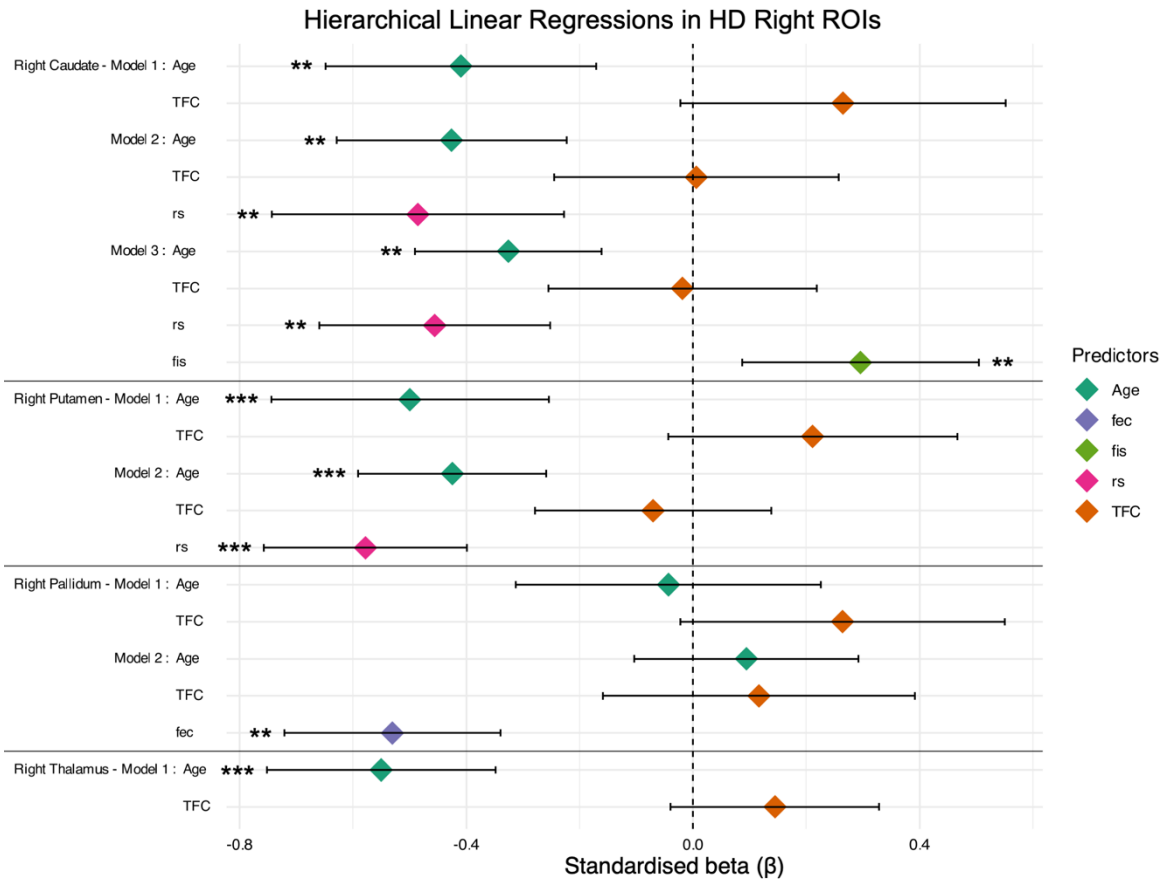
Hierarchical Linear Regressions in HD Right ROIs
Right Caudate - Model 1 : Age
TFC
Model 2 : Age
TFC
rs
Model 3 : Age
TFC
rs
fis
Right Putamen - Model 1 : Age
TFC
Model 2 : Age
TFC
rs
Right Pallidum - Model 1 : Age
TFC
Model 2 : Age
TFC
fec
Right Thalamus - Model 1 : Age
TFC
-0.8
-0.4
0.0
0.4
Standardised beta (β)
Predictors
Age
fec
fis
rs
TFC

Figure 8

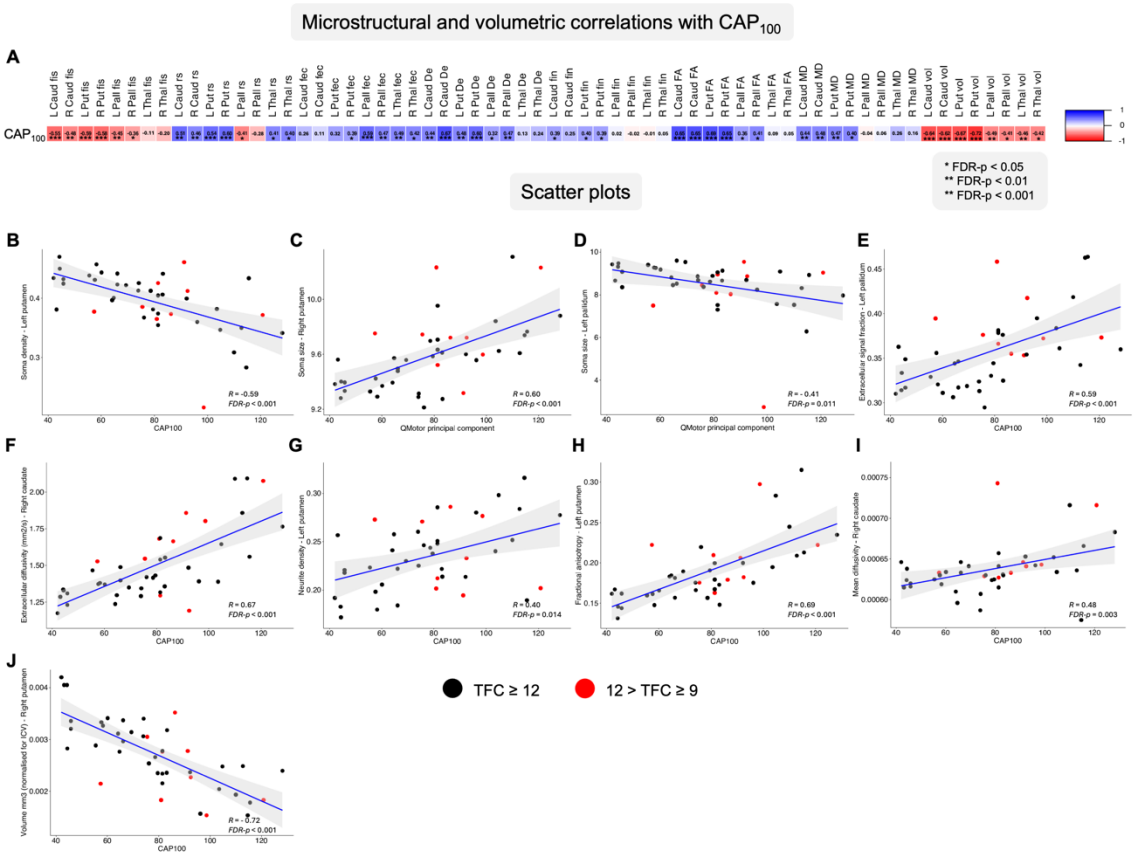
Microstructural and volumetric correlations with CAP100
A
CAP100
* FDR-p < 0.05
** FDR-p < 0.01
** FDR-p < 0.001
Scatter plots
B
C
D
E
F
G
H
I
J
TFC ≥ 12
12 > TFC ≥ 9

Figure legends

Figure 1. Volumetric differences in the basal ganglia and thalamus between HD-gene positive (HD) individuals and healthy controls (HC). Regions-of-interest (ROIs) were segmented using FreeSurfer v6. All ROIs, except the left thalamus, showed significantly smaller volumes in the HD cohort after FDR correction for multiple comparisons. Colours indicate the strength of rank-biserial correlations (r) from Mann-Whitney U tests: Red = strong effect ($r \geq 0.5$), Yellow = medium effect ($0.3 \leq r < 0.5$), White = small effect ($r < 0.3$). Raincloud plots show the distribution of the volumetric measures in each ROI per group with orange (HD gene=1) for HD-gene positive and green (HD gene=0) for HD-gene negative participants. * $p < 0.05$; *** $p < 0.001$

Figure 2. Microstructural differences in ROIs between HD-gene positive (HD) and healthy control (HC) groups. Median values of each microstructural measure were extracted per ROI. **A)** HD individuals show reduced soma density (f_{is}) in the basal ganglia (BG). **B)** Soma radius (r_s) is elevated in the caudate and putamen but reduced in the pallidum. **C)** Extracellular water fraction (f_{ec}) is increased in BG regions in the HD group. **D)** Extracellular diffusivity (D_e) is higher in the putamen and pallidum. **E)** Fractional anisotropy (FA) is elevated in the BG, and **F)** mean diffusivity (MD) is increased in the striatum. Colours represent rank-biserial correlations (r) from Mann-Whitney U tests: Red = strong effect ($r \geq 0.5$), Yellow = medium effect ($0.3 \leq r < 0.5$), White = small effect ($r < 0.3$). Raincloud plots show the distribution of the microstructural measures in each ROI per group with orange (HD gene=1) for HD-gene positive and green (HD gene=0) for HD-gene negative participants. * $p < 0.05$; ** $p < 0.01$; *** $p < 0.001$

Figure 3. A) Correlation matrix and **B-G)** selected scatter plots illustrating Spearman's rho correlations between SANDI measures and the Q-Motor principal component. **A)** Each cell represents the Spearman's rho correlation strength, with pink indicating negative and green positive correlations. **B-G)** Each plot includes a best-fit least squares linear regression line with standard error indicated by the grey shaded area, along with the Spearman's rho and the corresponding FDR-p value. Black dots represent participants with low disease burden (TFC scores of 12–13), while red dots indicate those with higher disease burden (TFC scores between 9 and 11). **Abbreviations:** $\mathbf{D_e}$: Extracellular diffusivity; $\mathbf{f_{ec}}$: Extracellular water signal fraction;

$\mathbf{f_{in}}$: Neurite density signal fraction; $\mathbf{f_{is}}$: Soma density signal fraction; **PC**: Principal component; $\mathbf{r_s}$: Soma radius; **TFC**: Total functional capacity.

Figure 4. A) Correlation matrix and **B-D)** selected scatter plots illustrating Spearman's rho correlations between DTI, volumetric measures and the Q-Motor principal component. **A)** Each cell represents the Spearman's rho correlation strength, with pink indicating negative and green positive correlations. **B-D)** Each plot includes a best-fit least squares linear regression line with standard error indicated by the grey shaded area, along with the Spearman's rho and the corresponding FDR-p value. Black dots represent participants with low disease burden (TFC scores of 12–13), while red dots indicate those with higher disease burden (TFC scores between 9 and 11). **Abbreviations: FA**: Fractional anisotropy; **MD**: Mean diffusivity.

Figure 5. Standardised beta coefficients of SANDI microstructural metrics predicting volume (normalised for intracranial volume) in regions of interest in the healthy control group. **Abbreviations: De**: Extracellular diffusivity; **fis**: Soma density signal fraction; **rs**: Soma radius; **TFC:** Total functional capacity. * $p < 0.05$; ** $p < 0.01$; *** $p < 0.001$.

Figure 6. Standardised beta coefficients of SANDI microstructural metrics predicting volume (normalised for intracranial volume) in left hemisphere regions of interest in Huntington's disease patients. **Abbreviations: De**: Extracellular diffusivity; **fec**: Extracellular water signal fraction; **fis**: Soma density signal fraction; **rs**: Soma radius. * $p < 0.05$; ** $p < 0.01$; *** $p < 0.001$.

Figure 7. Standardised beta coefficients of SANDI microstructural metrics predicting volume (normalised for intracranial volume) in right hemisphere regions of interest in Huntington's disease patients. **Abbreviations: fec**: Extracellular water signal fraction; **fis**: Soma density signal fraction; **rs**: Soma radius; **TFC:** Total functional capacity. * $p < 0.05$; ** $p < 0.01$; *** $p < 0.001$.

Figure 8. A) Correlation matrix and **B-J)** selected scatter plots illustrating Spearman's rho correlations between SANDI, DTI, and volumetric measures with CAP_{100}. Each scatter plot includes a best-fit least squares linear regression line with standard error indicated by the grey shaded area, along with the Spearman's rho (r) and the corresponding FDR-p value. Black dots represent participants with low disease burden (TFC scores of 12–13), while red dots indicate those with higher disease burden (TFC scores between 9 and 11). **Abbreviations: De**: Extracellular diffusivity; **FA**: Fractional anisotropy; **fec**: Extracellular water signal fraction;

fin: Neurite density signal fraction; **fis**: Soma density signal fraction; **MD**: Mean diffusivity; **rs**: Soma radius; **vol**: Normalised volume.

Data availability

This research utilised baseline data from the HD-DRUM project that has been endorsed by the Enroll-HD Scientific Oversight Committee (SOC) (14/11/2022). At the end of the HD-DRUM project, the coded study data will be shared and made accessible to the research community *via* the Enroll-HD specific data request process.

Acknowledgements

We would like to thank Lucy Layland, Amy Dangerfield, Allison Cooper and Sonya Foley-Bozorgzad for their help with data collection. We would like to thank the following clinical and administrative staff at the participating patient identification centres for their help with identifying suitable patients for the study: Eileen Donovan, Kim Munnery, and Jane Davies from the Cardiff HD clinic; Jessica Prado Mota from the Royal Devon University Healthcare NHS Foundation Trust in Exeter; Jenni Burns from the Walton Centre NHS Foundation Trust in Liverpool; Natalie Rosewell, Anya Soonderpershad, and Dr Liz Coulthard from the Bristol Brain Centre; Claire Tilley and Dr Hugh Rickards from the Birmingham and Solihull Mental Health NHS Foundation Trust. In addition, we would like to thank all Public Involvement contributors and the members of the Enroll-HD Scientific Oversight Committee for their input into the study as well as all participants for their generous time commitment to help us conducting this research.

Funding

This work was supported by a National Institute for Health Research (NIHR) and Health and Care Research Wales (HCRW) Advanced Fellowship to CM-B (grant number: NIHR-FS(A)-

2022). The Centre for Trials Research at Cardiff University receives infrastructure funding from HCRW. MP is supported by the UKRI Future Leaders Fellowship MR/T020296/2.

Competing interests

The authors have no conflicting interests to declare.

References

1. Rüb U, Seidel K, Heinsen H, Vonsattel JP, den Dunnen WF, Korf HW. Huntington's disease (HD): the neuropathology of a multisystem neurodegenerative disorder of the human brain. *Brain Pathology*. 2016;26(6):726-740. doi:10.1111/bpa.12426
2. Tabrizi SJ, Scahill RI, Durr A, et al. Biological and clinical changes in premanifest and early stage Huntington's disease in the TRACK-HD study: the 12-month longitudinal analysis. *Lancet Neurol*. 2011;10(1):31-42. doi:10.1016/S1474-4422(10)70276-3
3. Roos RAC. Huntington's disease: A clinical review. *Orphanet J Rare Dis*. 2010;5(1). doi:10.1186/1750-1172-5-40
4. Walker FO. Huntington's disease. *The Lancet*. 2007;369(9557):218-228. doi:10.1016/S0140-6736(07)60111-1
5. Ross CA, Aylward EH, Wild EJ, et al. Huntington disease: Natural history, biomarkers and prospects for therapeutics. *Nat Rev Neurol*. 2014;10(4):204-216. doi:10.1038/nrneurol.2014.24
6. Aylward EH, Liu D, Nopoulos PC, et al. Striatal volume contributes to the prediction of onset of Huntington disease in incident cases. *Biol Psychiatry*. 2012;71(9):822-828. doi:10.1016/j.biopsych.2011.07.030
7. Scahill RI, Zeun BMBS P, Osborne-Crowley K, et al. *Biological and Clinical Characteristics of Gene Carriers Far from Predicted Onset in the Huntington's Disease Young Adult Study (HD-YAS): A Cross-Sectional Analysis*. Vol 19.; 2020.
8. Tan B, Shishegar R, Poudel GR, Fornito A, Georgiou-Karistianis N. Cortical morphometry and neural dysfunction in Huntington's disease: a review. *Eur J Neurol*. 2021;28(4):1406-1419. doi:10.1111/ene.14648
9. Kinnunen KM, Schwarz AJ, Turner EC, et al. Volumetric MRI-Based Biomarkers in Huntington's Disease: An Evidentiary Review. *Front Neurol*. 2021;12(September). doi:10.3389/fneur.2021.712555
10. Wilkes FA, Abaryan Z, Ching CRK, et al. Striatal morphology and neurocognitive dysfunction in Huntington disease: The IMAGE-HD study. *Psychiatry Res Neuroimaging*. 2019;291(July):1-8. doi:10.1016/j.pscychresns.2019.07.003
11. Paulsen JS, Langbehn DR, Stout JC, et al. Detection of Huntington's disease decades before diagnosis: The Predict-HD study. *J Neurol Neurosurg Psychiatry*. 2008;79(8):874-880. doi:10.1136/jnnp.2007.128728
12. Biglan KM, Zhang Y, Long JD, et al. Refining the diagnosis of huntington disease: The PREDICT-HD study. *Front Aging Neurosci*. 2013;5(APR):1-8. doi:10.3389/fnagi.2013.00012
13. Tabrizi SJ, Langbehn DR, Leavitt BR, et al. Biological and clinical manifestations of Huntington's disease in the longitudinal TRACK-HD study: cross-sectional analysis of baseline data. *Lancet Neurol*. 2009;8(9):791-801. doi:10.1016/S1474-4422(09)70170-X
14. Tabrizi SJ, Reilmann R, Roos RA, et al. Potential endpoints for clinical trials in premanifest and early Huntington's disease in the TRACK-HD study: analysis of 24

month observational data. *Lancet Neurol*. 2012;11(1):42-53. doi:10.1016/S1474-4422(11)70263-0
15. Tabrizi SJ, Scahill RI, Owen G, et al. Predictors of phenotypic progression and disease onset in premanifest and early-stage Huntington's disease in the TRACK-HD study: Analysis of 36-month observational data. *Lancet Neurol*. 2013;12(7):637-649. doi:10.1016/S1474-4422(13)70088-7
16. Tabrizi SJ, Estevez-Fraga C, van Roon-Mom WMC, et al. Potential disease-modifying therapies for Huntington's disease: lessons learned and future opportunities. *Lancet Neurol*. 2022;21(7):645-658. doi:10.1016/S1474-4422(22)00121-1
17. Vonsattel PJG, Keller C, Cortes Ramirez PE. Huntington's disease-neuropathology. In: *Handbook of Clinical Neurology*. Vol 100. ; 2011:83-100.
18. Liu CF, Younes L, Tong XJ, et al. Longitudinal imaging highlights preferential basal ganglia circuit atrophy in Huntington's disease. *Brain Commun*. 2023;5(5). doi:10.1093/braincomms/fcad214
19. Johnson EB, Ziegler G, Penny W, et al. Dynamics of Cortical Degeneration Over a Decade in Huntington's Disease. *Biol Psychiatry*. 2021;89(8):807-816. doi:10.1016/j.biopsych.2020.11.009
20. Estevez-Fraga C, Scahill R, Rees G, Tabrizi SJ, Gregory S. Diffusion imaging in Huntington's disease: Comprehensive review. *J Neurol Neurosurg Psychiatry*. 2021;92(1):62-69. doi:10.1136/jnnp-2020-324377
21. Tabrizi SJ, Schobel S, Gantman EC, et al. A biological classification of Huntington's disease: the Integrated Staging System. *Lancet Neurol*. 2022;21(7):632-644. doi:10.1016/S1474-4422(22)00120-X
22. Myers RH, Vonsattel JP, Paskevich PA, et al. Decreased Neuronal and Increased Oligodendroglial Densities in Huntington's Disease Caudate Nucleus. *J Neuropathol Exp Neurol*. 1991;50(6):729-742. doi:10.1097/00005072-199111000-00005
23. Vis JC, Schipper E, de Boer-van H, et al. Expression pattern of apoptosis-related markers in Huntington's disease. *Acta Neuropathol*. 2005;109(3):321-328. doi:10.1007/s00401-004-0957-5
24. Vis JC, Nicholson LFB, Faull RLM, Evans WH, Severs NJ, Green CR. Connexin expression in Huntington's diseased human brain. *Cell Biol Int*. 1998;22(11-12):837-847. doi:10.1006/cbir.1998.0388
25. Simmons DA, Casale M, Alcon B, Pham N, Narayan N, Lynch G. Ferritin accumulation in dystrophic microglia is an early event in the development of Huntington's Disease. *Glia*. 2007;55(10):1074-1084. doi:10.1002/glia.20526
26. Sapp E, Kegel KB, Aronin N, et al. Early and Progressive Accumulation of Reactive Microglia in the Huntington Disease Brain. *J Neuropathol Exp Neurol*. 2001;60(2):161-172. doi:10.1093/jnen/60.2.161
27. Palombo M, Ianus A, Guerreri M, et al. SANDI: A compartment-based model for non-invasive apparent soma and neurite imaging by diffusion MRI. *Neuroimage*. 2020;215(August 2019):116835. doi:10.1016/j.neuroimage.2020.116835
28. Le Bihan D, Turner R, Moonen CTW, Pekar J. Imaging of diffusion and microcirculation with gradient sensitization: Design, strategy, and significance.

Journal of Magnetic Resonance Imaging. 1991;1(1):7-28. doi:10.1002/jmri.1880010103
29. Basser PJ, Mattiello J, LeBihan D. MR diffusion tensor spectroscopy and imaging. *Biophys J*. 1994;66(1):259-267. doi:10.1016/S0006-3495(94)80775-1
30. Basser PJ, Pierpaoli C. Microstructural and Physiological Features of Tissues Elucidated by Quantitative-Diffusion-Tensor MRI. *J Magn Reson B*. 1996;111(3):209-219. doi:10.1006/jmrb.1996.0086
31. Georgiou-Karistianis N, Grey MA, Domínguez D JF, et al. Automated differentiation of pre-diagnosis Huntington's disease from healthy control individuals based on quadratic discriminant analysis of the basal ganglia: The IMAGE-HD study. *Neurobiol Dis*. 2013;51:82-92. doi:10.1016/j.nbd.2012.10.001
32. Hobbs NZ, Cole JH, Farmer RE, et al. Evaluation of multi-modal, multi-site neuroimaging measures in Huntington's disease: Baseline results from the PADDINGTON study. *Neuroimage Clin*. 2013;2(1):204-211. doi:10.1016/j.nicl.2012.12.001
33. Jones DK, Alexander DC, Bowtell R, et al. Microstructural imaging of the human brain with a 'super-scanner': 10 key advantages of ultra-strong gradients for diffusion MRI. *Neuroimage*. 2018;182(May):8-38. doi:10.1016/j.neuroimage.2018.05.047
34. Assaf Y, Basser PJ. Composite hindered and restricted model of diffusion (CHARMED) MR imaging of the human brain. *Neuroimage*. 2005;27(1):48-58. doi:10.1016/j.neuroimage.2005.03.042
35. Zhang H, Schneider T, Wheeler-Kingshott CA, Alexander DC. NODDI: Practical in vivo neurite orientation dispersion and density imaging of the human brain. *Neuroimage*. 2012;61(4):1000-1016. doi:10.1016/j.neuroimage.2012.03.072
36. Martinez-Heras E, Grussu F, Prados F, Solana E, Llufriu S. Diffusion-Weighted Imaging: Recent Advances and Applications. *Seminars in Ultrasound, CT and MRI*. 2021;42(5):490-506. doi:10.1053/j.sult.2021.07.006
37. Daducci A, Dal Palu A, Lemkaddem A, Thiran JP. COMMIT: Convex Optimization Modeling for Microstructure Informed Tractography. *IEEE Trans Med Imaging*. 2015;34(1):246-257. doi:10.1109/TMI.2014.2352414
38. Zhang J, Gregory S, Scahill RI, et al. In vivo characterization of white matter pathology in premanifest huntington's disease. *Ann Neurol*. 2018;84(4):497-504. doi:10.1002/ana.25309
39. Koller K, Rudrapatna U, Chamberland M, et al. MICRA: Microstructural image compilation with repeated acquisitions. *Neuroimage*. 2021;225(October 2020):117406. doi:10.1016/j.neuroimage.2020.117406
40. Ianuş A, Carvalho J, Fernandes FF, et al. Soma and Neurite Density MRI (SANDI) of the in-vivo mouse brain and comparison with the Allen Brain Atlas. *Neuroimage*. 2022;254. doi:10.1016/j.neuroimage.2022.119135
41. Krijnen EA, Russo AW, Salim Karam E, et al. Detection of grey matter microstructural substrates of neurodegeneration in multiple sclerosis. *Brain Commun*. 2023;5(3). doi:10.1093/braincomms/fcad153

42. Margoni M, Pagani E, Preziosa P, et al. In vivo quantification of brain soma and neurite density abnormalities in multiple sclerosis. *J Neurol*. 2023;270(1):433-445. doi:10.1007/s00415-022-11386-3
43. Barakovic M, Weigel M, Cagol A, et al. A novel imaging marker of cortical "cellularity" in multiple sclerosis patients. *Sci Rep*. 2024;14(1):9848. doi:10.1038/s41598-024-60497-6
44. Byrne LM, Rodrigues FB, Johnson EB, et al. *Evaluation of Mutant Huntingtin and Neurofilament Proteins as Potential Markers in Huntington's Disease*. Vol 10.; 2018. https://www.science.org
45. Sampedro F, Pérez-Pérez J, Martínez-Horta S, et al. Cortical microstructural correlates of plasma neurofilament light chain in Huntington's disease. *Parkinsonism Relat Disord*. 2021;85:91-94. doi:10.1016/j.parkreldis.2021.03.008
46. Schiavi S, Palombo M, Zacà D, et al. Mapping tissue microstructure across the human brain on a clinical scanner with soma and neurite density image metrics. *Hum Brain Mapp*. 2023;44(13):4792-4811. doi:10.1002/hbm.26416
47. Olesen JL, Østergaard L, Shemesh N, Jespersen SN. Diffusion time dependence, power-law scaling, and exchange in grey matter. *Neuroimage*. 2022;251:118976. doi:10.1016/j.neuroimage.2022.118976
48. Jelescu IO, de Skowronski A, Geffroy F, Palombo M, Novikov DS. Neurite Exchange Imaging ((NEXI): A minimal model of diffusion in grey matter with inter-compartment water exchange. *Neuroimage*. 2022;256. doi:10.1016/j.neuroimage.2022.119277
49. Bechtel N, Scahill RI, Rosas HD, et al. Tapping linked to function and structure in premanifest and symptomatic Huntington disease. *Neurology*. 2010;75(24):2150-2160. doi:10.1212/WNL.0b013e3182020123
50. Schubert R, Fiedler H, Barallon P, Habbel B, Reilmann R. F55 Q-motor speeded tapping and pointing assessments: feasibility of a dual task design. In: *F: Clinical Studies: Case Reports, Observational Studies and Trials*. BMJ Publishing Group Ltd; 2022:A56.1-A56. doi:10.1136/jnnp-2022-ehdn.146
51. Schubert R, Rosser A, Bachoud-Lévi AC, Craufurd D, Reilmann R. F63 Preliminary results from Q-MOTOR/Q-COG analyses in the repair-hd study. In: *Clinical Studies*. BMJ Publishing Group Ltd; 2018:A62.1-A62. doi:10.1136/jnnp-2018-EHDN.164
52. Reilmann R, Schubert R. *Motor Outcome Measures in Huntington Disease Clinical Trials*. Vol 144. 1st ed. Elsevier B.V.; 2017. doi:10.1016/B978-0-12-801893-4.00018-3
53. Reilmann R, Rosser A, Kostyk S, et al. F41 The proof-hd phase 3 study: pridopidine's outcome on function in huntington disease (PROOF). In: *F: Clinical Studies: Case Reports, Observational Studies and Trials*. BMJ Publishing Group Ltd; 2021:A36.1-A36. doi:10.1136/jnnp-2021-EHDN.84
54. Reilmann R, Anderson KE, Feigin A, et al. Safety and efficacy of laquinimod for Huntington's disease (LEGATO-HD): a multicentre, randomised, double-blind, placebo-controlled, phase 2 study. *Lancet Neurol*. 2024;23(3):243-255. doi:10.1016/S1474-4422(23)00454-4
55. Farag M, Knights H, Scahill RI, McColgan P, Estevez-Fraga C. Neuroimaging Techniques in Huntington's Disease: A Critical Review. *Mov Disord Clin Pract*. Published online 2025. doi:10.1002/mdc3.70010

56. Ioakeimidis V, Busse M, Drew CJG, et al. Protocol for a randomised controlled unblinded feasibility trial of HD-DRUM: a rhythmic movement training application for cognitive and motor symptoms in people with Huntington's disease. *BMJ Open*. 2024;14(7):e082161. doi:10.1136/bmjopen-2023-082161
57. Casella C, Chamberland M, Laguna PL, et al. Mutation-related magnetization-transfer, not axon density, drives white matter differences in premanifest Huntington disease: Evidence from in vivo ultra-strong gradient MRI. *Hum Brain Mapp*. 2022;(October 2021):3439-3460. doi:10.1002/hbm.25859
58. McNabb CB, Driver ID, Hyde V, et al. WAND: A multi-modal dataset integrating advanced MRI, MEG, and TMS for multi-scale brain analysis. *Sci Data*. 2025;12(1):220. doi:10.1038/s41597-024-04154-7
59. Siesling S, Van Vugt JPP, Zwinderman KAH, Kieburtz K, Roos RAC. Unified Huntington's disease rating scale: A follow up. *Movement Disorders*. 1998;13(6):915-919. doi:10.1002/mds.870130609
60. Sathe S, Ware J, Levey J, et al. Enroll-HD: An Integrated Clinical Research Platform and Worldwide Observational Study for Huntington's Disease. *Front Neurol*. 2021;12. doi:10.3389/fneur.2021.667420
61. Nasreddine ZS, Phillips NA, Bédirian V, et al. The Montreal Cognitive Assessment, MoCA: A Brief Screening Tool For Mild Cognitive Impairment. *J Am Geriatr Soc*. 2005;53(4):695-699. doi:10.1111/j.1532-5415.2005.53221.x
62. Wechsler D. Test of Premorbid Functioning. UK version (TOPF UK). Published online 2011.
63. Warner JH, Long JD, Mills JA, et al. Standardizing the CAP Score in Huntington's Disease by Predicting Age-at-Onset. *J Huntingtons Dis*. 2022;11(2):153-171. doi:10.3233/JHD-210475
64. Hermle D, Schubert R, Barallon P, et al. Multifeature quantitative motor assessment of upper limb ataxia including drawing and reaching. *Ann Clin Transl Neurol*. 2024;11(5):1097-1109. doi:10.1002/acn3.52024
65. Tuch DS, Reese TG, Wiegell MR, Makris N, Belliveau JW, Wedeen VJ. High angular resolution diffusion imaging reveals intravoxel white matter fiber heterogeneity. *Magn Reson Med*. 2002;48(4):577-582. doi:10.1002/mrm.10268
66. Smith SM. Fast robust automated brain extraction. *Hum Brain Mapp*. 2002;17(3):143-155. doi:10.1002/hbm.10062
67. Tournier JD, Smith R, Raffelt D, et al. MRtrix3: A fast, flexible and open software framework for medical image processing and visualisation. *Neuroimage*. 2019;202:116137. doi:10.1016/j.neuroimage.2019.116137
68. Leemans A, Jeurissen B, Sijbers J, Jones DK. ExploreDTI: a graphical toolbox for processing, analyzing, and visualizing diffusion MR data . In: *ISMRM*. ; 2009.
69. Sairanen V, Leemans A, Tax CMW. Fast and accurate Slicewise OutLIer Detection (SOLID) with informed model estimation for diffusion MRI data. *Neuroimage*. 2018;181:331-346. doi:10.1016/j.neuroimage.2018.07.003
70. Andersson JLR, Skare S, Ashburner J. How to correct susceptibility distortions in spin-echo echo-planar images: application to diffusion tensor imaging. *Neuroimage*. 2003;20(2):870-888. doi:10.1016/S1053-8119(03)00336-7

71. Smith SM, Jenkinson M, Woolrich MW, et al. Advances in functional and structural MR image analysis and implementation as FSL. *Neuroimage*. 2004;23:S208-S219. doi:10.1016/j.neuroimage.2004.07.051
72. Andersson JLR, Sotiropoulos SN. An integrated approach to correction for off-resonance effects and subject movement in diffusion MR imaging. *Neuroimage*. 2016;125:1063-1078. doi:10.1016/j.neuroimage.2015.10.019
73. Kellner E, Dhital B, Kiselev VG, Reisert M. Gibbs-ringing artifact removal based on local subvoxel-shifts. *Magn Reson Med*. 2016;76(5):1574-1581. doi:10.1002/mrm.26054
74. Cordero-Grande L, Christiaens D, Hutter J, Price AN, Hajnal J V. Complex diffusion-weighted image estimation via matrix recovery under general noise models. *Neuroimage*. 2019;200:391-404. doi:10.1016/j.neuroimage.2019.06.039
75. Veraart J, Fieremans E, Novikov DS. Diffusion MRI noise mapping using random matrix theory. *Magn Reson Med*. 2016;76(5):1582-1593. doi:10.1002/mrm.26059
76. Veraart J, Novikov DS, Christiaens D, Ades-aron B, Sijbers J, Fieremans E. Denoising of diffusion MRI using random matrix theory. *Neuroimage*. 2016;142:394-406. doi:10.1016/j.neuroimage.2016.08.016
77. Fischl B. FreeSurfer. *Neuroimage*. 2012;62(2):774-781. doi:10.1016/j.neuroimage.2012.01.021
78. Jenkinson M. Improved Optimization for the Robust and Accurate Linear Registration and Motion Correction of Brain Images. *Neuroimage*. 2002;17(2):825-841. doi:10.1016/S1053-8119(02)91132-8
79. JASP Team. JASP. Published online 2023.
80. R Core Team. R: A Language and Environment for Statistical Computing. Published online 2024.
81. RStudio Team. RStudio: Integrated Development for R. Published online 2024.
82. IBM Corp. IBM SPSS Statistics for Windows. Published online 2024.
83. Preacher KJ, MacCallum RC. Exploratory Factor Analysis in Behavior Genetics Research: Factor Recovery with Small Sample Sizes. *Behav Genet*. 2002;32(2):153-161. doi:10.1023/A:1015210025234
84. de Winter JCF, Dodou D, Wieringa PA. Exploratory Factor Analysis With Small Sample Sizes. *Multivariate Behav Res*. 2009;44(2):147-181. doi:10.1080/00273170902794206
85. Benjamini Y, Hochberg Y. Controlling the False Discovery Rate: A Practical and Powerful Approach to Multiple Testing. *J R Stat Soc Series B Stat Methodol*. 1995;57(1):289-300. doi:10.1111/j.2517-6161.1995.tb02031.x
86. Lakens D. Performing high-powered studies efficiently with sequential analyses. *Eur J Soc Psychol*. 2014;44(7):701-710. doi:10.1002/ejsp.2023
87. Matz OC, Spocter M. The Effect of Huntington's Disease on the Basal Nuclei: A Review. *Cureus*. Published online April 25, 2022. doi:10.7759/cureus.24473
88. Sánchez-Castañeda C, Cherubini A, Elifani F, et al. Seeking huntington disease biomarkers by multimodal, cross-sectional basal ganglia imaging. *Hum Brain Mapp*. 2013;34(7):1625-1635. doi:10.1002/hbm.22019

89. Fricker M, Tolkovsky AM, Borutaite V, Coleman M, Brown GC. Neuronal Cell Death. *Physiol Rev*. 2018;98(2):813-880. doi:10.1152/physrev.00011.2017
90. Kerr JFR, Wyllie AH, Currie AR. Apoptosis: A Basic Biological Phenomenon with Wideranging Implications in Tissue Kinetics. *Br J Cancer*. 1972;26(4):239-257. doi:10.1038/bjc.1972.33
91. Klaus A, Alves da Silva J, Costa RM. What, If, and When to Move: Basal Ganglia Circuits and Self-Paced Action Initiation. *Annu Rev Neurosci*. 2019;42(1):459-483. doi:10.1146/annurev-neuro-072116-031033